Original Research

Dynamic Perfusion MRI: Capability for Evaluation of Disease Severity and Progression of Pulmonary Arterial Hypertension in Patients With Connective Tissue Disease

Yoshiharu Ohno, MD, PhD,[1*] Hisanobu Koyama, MD,[1] Munenobu Nogami, MD, PhD,[1,2] Daisuke Takenaka, MD,[1] Sumiaki Matsumoto, MD, PhD,[1] Yumiko Onishi, MD,[1,2] Keiko Matsumoto, MD,[1,3] Kenya Murase, PhD,[4] and Kazuro Sugimura, MD[1]

Purpose: To prospectively evaluate the capability of dynamic perfusion MRI for assessment of disease severity and progression to pulmonary arterial hypertension (PAH) in connective tissue disease (CTD) patients.

Materials and Methods: In all, 18 gender- and age-matched CTD patients without and with PAH and nine healthy volunteers underwent dynamic perfusion MRI, Doppler echocardiography, and pulmonary function test. Disease severity of CTD was assessed in terms of diffusing capacity for carbon monoxide (%DL_{CO}) and estimated systolic pulmonary arterial pressure (sPAP), and progression of PAH in terms of pulmonary arterial pressure (mPAP) and pulmonary vascular resistance (PVR). From calculated pulmonary perfusion parameter maps, means of pulmonary blood flow (mPBF), pulmonary blood volume (mPBV), and mean transit time (mMTT) were determined as averages of all region of interest (ROI) measurements. To determine disease severity in CTD, all parameters were statistically correlated with sPAP and %DL_{CO}. To determine progression to PAH, all parameters were statistically correlated with mPAP and PVR.

Results: All pulmonary perfusion parameters correlated significantly with sPAP and %DL_{CO} ($P < 0.05$). mPBF and mPBV correlated significantly with mPAP and moderately with PVR ($P < 0.05$).

Conclusion: Dynamic perfusion MRI can be used for assessment of disease severity and progression of PAH in CTD patients.

Key Words: lung; CT; MR; perfusion; interstitial lung disease; hypertension
J. Magn. Reson. Imaging 2008;28:887–899.

PULMONARY COMPLICATIONS are common in patients with connective tissue disease (CTD). They may occur as a result of underlying disease or as a complication related to treatment. Although interstitial lung disease is the most common pulmonary complication of CTD, pulmonary vascular involvement may also manifest itself as alveolar hemorrhage or as pulmonary hypertension (PAH). The occurrence of PAH has been reported in association with every known type of collagen vascular disease. However, the frequency of pulmonary hypertension varies substantially among CTD patients.

PAH is generally known as a rare complication of rheumatoid arthritis, dermatomyositis, and polymyositis (1). Rapidly progressive pulmonary hypertension may accompany Sjögren's syndrome, but this is also a very rare complication (1). Pulmonary hypertension is found in 5%–10% of all patients with systemic lupus erythematosus (1), while PAH may occur in 10%–33% of patients with systemic sclerosis (1–3), and this ratio may be even higher in patients with mixed connective tissue disease (MCTD) (1,4,5). In cases with the calcinosis, Raynouds phenomenon, esophageal involvement, sclerodactyly, and telangiectasia (CREST) syndrome (currently referred to as limited systemic sclerosis), the incidence of PAH ranges from 10%–30%, and an autopsy study found changes compatible with PAH in as many as 50% of patients with limited sys-

[1]Department of Radiology, Kobe University Graduate School of Medicine, Kobe, Japan.
[2]Division of Image-Based Medicine, Institute of Biomedical Research and Innovation, Kobe, Japan.
[3]Department of Radiology, University of Yamanashi, Chuoh, Japan.
[4]Department of Medical Physics and Engineering, Division of Medical Technology and Science, Faculty of Health Science, Graduate School of Medicine, Osaka University, Osaka, Japan.
Contract grant sponsor: Daiichi-Sankyo Co. Ltd.,; Contract grant sponsor: Philips Healthcare; Contract grant sponsor: Knowledge Cluster Initiative of the Ministry of Education, Culture, Sports, Science and Technology, Japan.
*Address reprint requests to: Y.O., Department of Radiology, Kobe University Graduate School of Medicine, 7-5-1 Kusunoki-cho, Chuo-ku, Kobe 650-0017, Japan. E-mail: yosirad@med.kobe-u.ac.jp or yosirad@kobe-u.ac.jp or yoshiharuohno@aol.com
Received April 1, 2008; Accepted July 11, 2008.
DOI 10.1002/jmri.21550
Published online in Wiley InterScience (www.interscience.wiley.com).

temic sclerosis (1,5). In addition, the development of pulmonary hypertension is an ominous prognostic sign. Therefore, assessment of PAH in some types of CTD such as systemic sclerosis and MCTD is vital for an accurate prognosis.

Although several radiological methods such as computed tomography (CT) and velocity-encoded magnetic resonance imaging (MRI) using the phase-contrast MR technique can help evaluate the severity of pulmonary hypertension (6–9), the Doppler cardiac echogram has been the most frequently utilized for assessment of PAH in clinical situations. This modality has been adopted as a noninvasive method for assessment of mean pulmonary arterial pressure (mPAP) and pulmonary vascular resistance (PVR). In addition, perfusion scintigraphy is the only radiological method commonly used for quantitative and qualitative assessment of pulmonary perfusion abnormalities in primary PAH patients (10,11).

Recently, a 3D dynamic contrast-enhanced MR perfusion imaging (3D dynamic perfusion MRI) method can qualitatively evaluate regional perfusion differences in the entire lung with high temporal and spatial resolutions (12–14). Moreover, when combined with the indicator dilution theory and fuzzy cluster analysis, this method can be used for quantitative assessment of regional pulmonary perfusion abnormalities in lung cancer, chronic obstructive lung disease, and PAH patients, prediction of postoperative lung function in lung cancer patients (15–19), and evaluation of disease severity in primary PAH patients (17,18). In addition, injection protocols using a small amount of bolus have also been proposed for accurate and reproducible perfusion measurements (20–22).

In the current study we hypothesized that quantitatively assessed 3D dynamic perfusion MRI may be useful for assessment of disease severity and progression of PAH in CTD patients. The purpose of our study was thus to evaluate the ability of this method to assess disease severity and progression to PAH in CTD patients.

MATERIALS AND METHODS

Subjects

The Institutional Review Board at our institution approved this study and informed consent was obtained from each subject prior to enrolment in the study.

A total of 72 consecutive CTD patients (59 women and 13 men, age 32–73 years; mean age: 57 years) underwent Doppler echocardiography and the pulmonary function test and the results were used to divide the patients into two groups (CTD with PAH and CTD without PAH). All CTD patients with estimated systolic pulmonary arterial pressure (sPAP) >35 mmHg and/or tricuspid velocity >3.4 m/s on their Doppler echocardiogram were suspected of having PAH (23) and underwent right heart catheterizations within 3 weeks (mean 11 days). No changes in drug treatment or clinically important evolution of the disease occurred during this time. Finally, PAH was defined as either mean pulmonary arterial pressure (mPAP) >25 mmHg at rest or mPAP >30 mmHg with exercise accompanied by a normal pulmonary capillary wedge pressure (PCWP) of <15 mmHg (to exclude left heart disease) (23,24). In 72 CTD patients, nine patients (seven women and two men, age 45–69 years; mean age: 58 years) were diagnosed as CTD patients with PAH and 63 patients (52 women and 11 men, age 32–73 years; mean age: 57 years) were diagnosed as CTD patients without PAH.

Next, 18 gender- and age-matched CTD patients, nine without PAH (seven women and two men, age 45–69 years; mean age: 58 years) and nine with PAH (seven women and two men, age 32–67 years; mean age: 55 years), as well as nine normal healthy volunteers (seven women and two men, age 38–66 years; mean age: 54 years) were prospectively selected. They all underwent thin-section CT, 3D dynamic perfusion MRI, Doppler echocardiography, and a pulmonary function test within 72 hours (mean, 26 hours). No change in drug treatment or clinically important evolution of the disease occurred during these examinations. Of the 18 CTD patients, 16 were diagnosed with systemic sclerosis and two with MCTD based on criteria for systemic sclerosis (25–27) and MCTD (28,29).

Dynamic Contrast-Enhanced MRI

All MR studies were performed on a 1.5T superconducting magnet (Gyroscan Intera; Philips Healthcare, Best, The Netherlands) using a phased-array coil. Dynamic MR images (TR/TE 2.7/0.6 msec, flip angle 40°, 128 × 96 matrix, 256 × 192 reconstructed matrix, rectangular field of view (FOV); 450–530 × 315–371 mm) were acquired with a 3D radiofrequency spoiled GRE sequence. For each examination, a 3D slab thickness of 120–240 mm with 10–12 partitions was used with an overcontiguous slice technique in the coronal plane and left-to-right phase encoding, resulting in an effective partition thickness of 10–20 mm and real phase encoding in the slice direction of five to six steps. The temporal resolution was 1.1 seconds for each 3D dataset.

In each subject with body weight less than 70 kg, 5 mL of gadodiamide hydrate (Gd-DTPA BMA, Omniscan; Daiichi-Sankyo, Tokyo, Japan) with 0.3 mmol/mL was administered via a cubital vein by means of an automatic infusion system (Sonic shot; Nemoto, Tokyo, Japan) at a rate of 5 mL/sec, followed by 20 mL of saline solution at the same rate. On the other hand, in each subject with body weight equal to or more than 70 kg, 5 mL of the same contrast media with 0.5 mmol/mL was administered via a cubital vein by means of the same automatic infusion system at a rate of 5 mL/sec, followed by 20 mL of saline solution at the same rate. The basic theory and application of contrast-enhanced dynamic perfusion MRI has been documented in previous reports (12–22). After careful instruction, patients practiced the breath-holding technique to reproduce a consistent degree of inspiration for each scan series before the MR studies. For each scan, 20 images were obtained at end-inspiration of a single breath-hold.

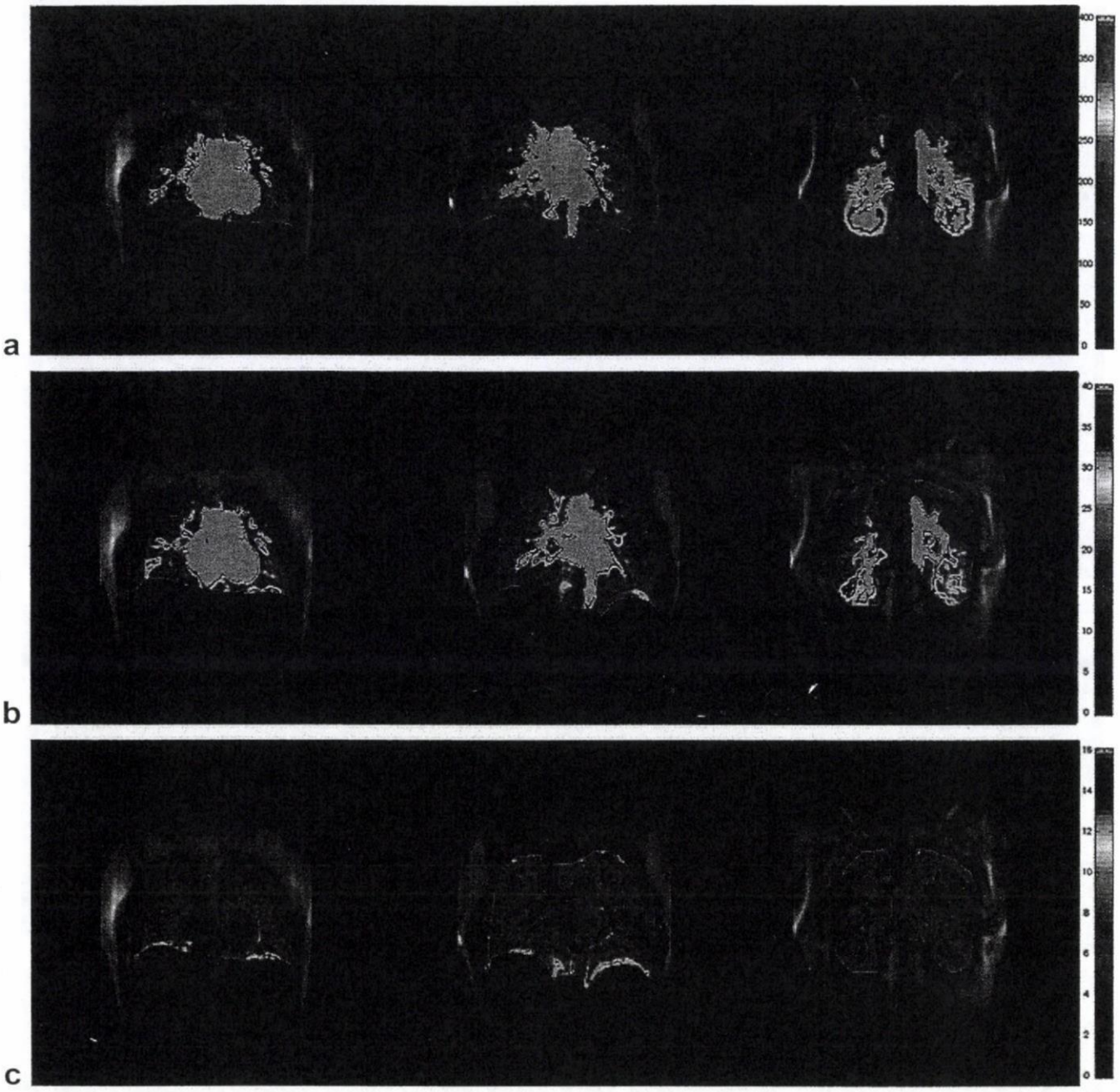

Figure 1. Quantitative pulmonary perfusion parameter maps for a 52-year-old female healthy volunteer. **a:** Image maps (L to R: ventral to dorsal) of PBF from coronal 3D dynamic MR data show regional changes in PBF in the gravitational and isogravitational directions. mPBF was 154.4 ± 25.3/100 mL/min. **b:** Image maps (L to R: ventral to dorsal) of PBV from coronal 3D dynamic MR data show regional changes in PBV in the gravitational and isogravitational directions. mPBV was 12.8 ± 3.2/100 mL. **c:** Image maps (L to R: ventral to dorsal) of MTT from coronal 3D dynamic MR data show regional changes in MTT in the gravitational and isogravitational directions. mMTT was 5.0 ± 0.6 seconds.

Data Analysis of Dynamic Contrast-Enhanced MR Perfusion Imaging

All pulmonary perfusion parameters on dynamic contrast-enhanced MR perfusion imaging were analyzed with previously reported methods using proprietary software developed for MatLab (MathWorks, Natick, MA) and run on a personal computer (Dell Precision 690; DELL, Round Rock, TX).

The signal intensity for every voxel in each slice of dynamic MR data was measured. According to the indicator dilution theory (30) for intravascular contrast agents, when the arterial input function (AIF) of the contrast agent entering the volume of interest (VOI) is known, the pulmonary blood flow (PBF) is implicitly given by the equation:

$$C_{VOI}(t) = PBF \int_0^t C_{AIF}(\tau) \times R(t - \tau) d\tau \qquad [1]$$

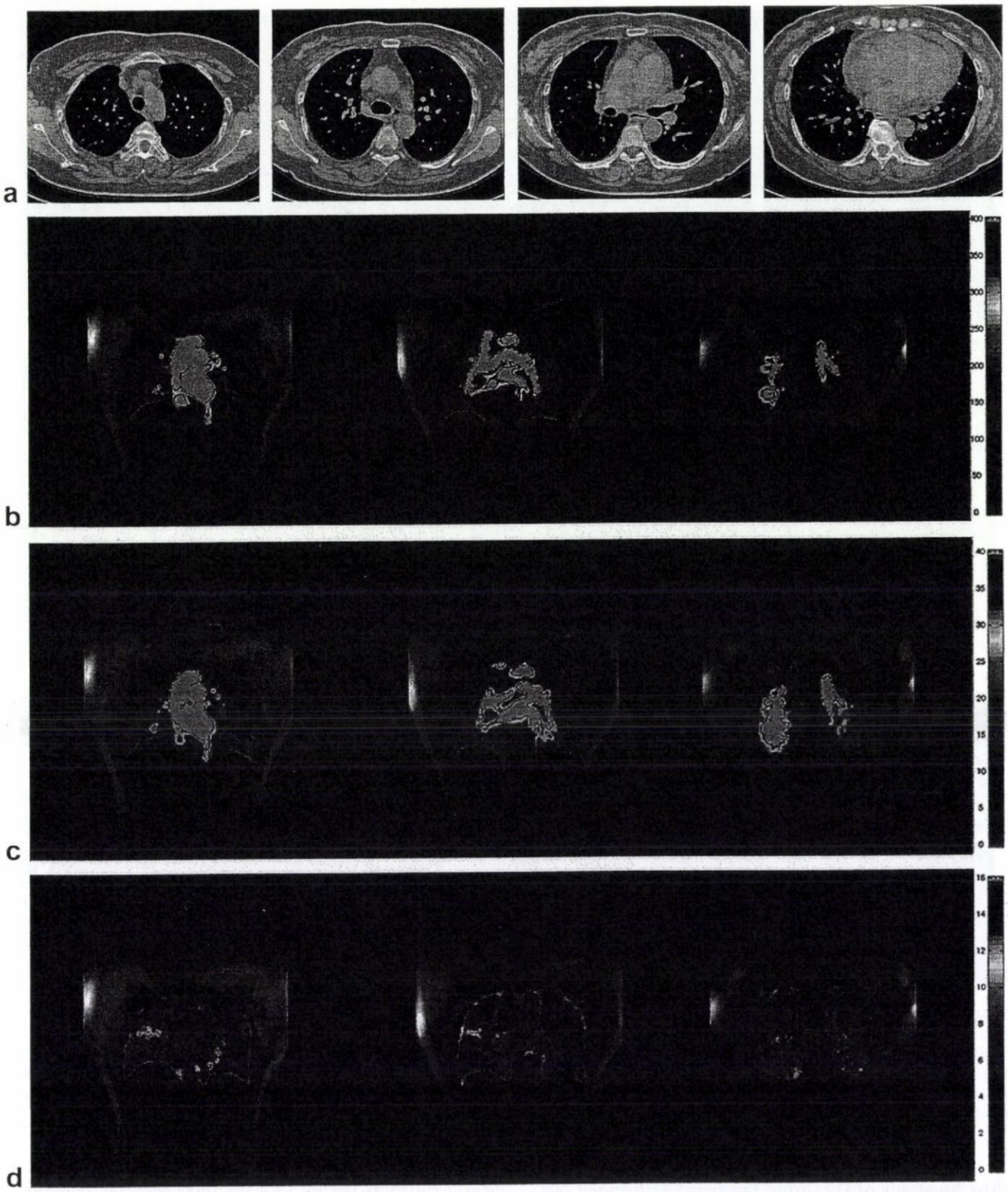

Figure 2. Quantitative pulmonary perfusion parameter maps for a 45-year-old female CTD patient without PAH. **a:** Thin-section CT images (L to R: cranial to caudal) demonstrate ground-glass attenuations and irregular pleural margin in the both lungs. CT-based disease severity was assessed as 9. **b:** Image maps (L to R: ventral to dorsal) of PBF from coronal 3D dynamic MR data show heterogeneously reduced regional PBF in the gravitational and isogravitational directions. mPBF was 135.8 ± 29.4/100 mL/min. **c:** Image maps (L to R: ventral to dorsal) of PBV from coronal 3D dynamic MR data show heterogeneously reduced regional PBV in the gravitational and isogravitational directions. mPBV was 12.4 ± 3.9/100 mL. **d:** Image maps (L to R: ventral to dorsal) of MTT from coronal 3D dynamic MR data show heterogeneously changed regional MTT in the gravitational and isogravitational directions. mMTT was 5.5 ± 1.2 seconds.

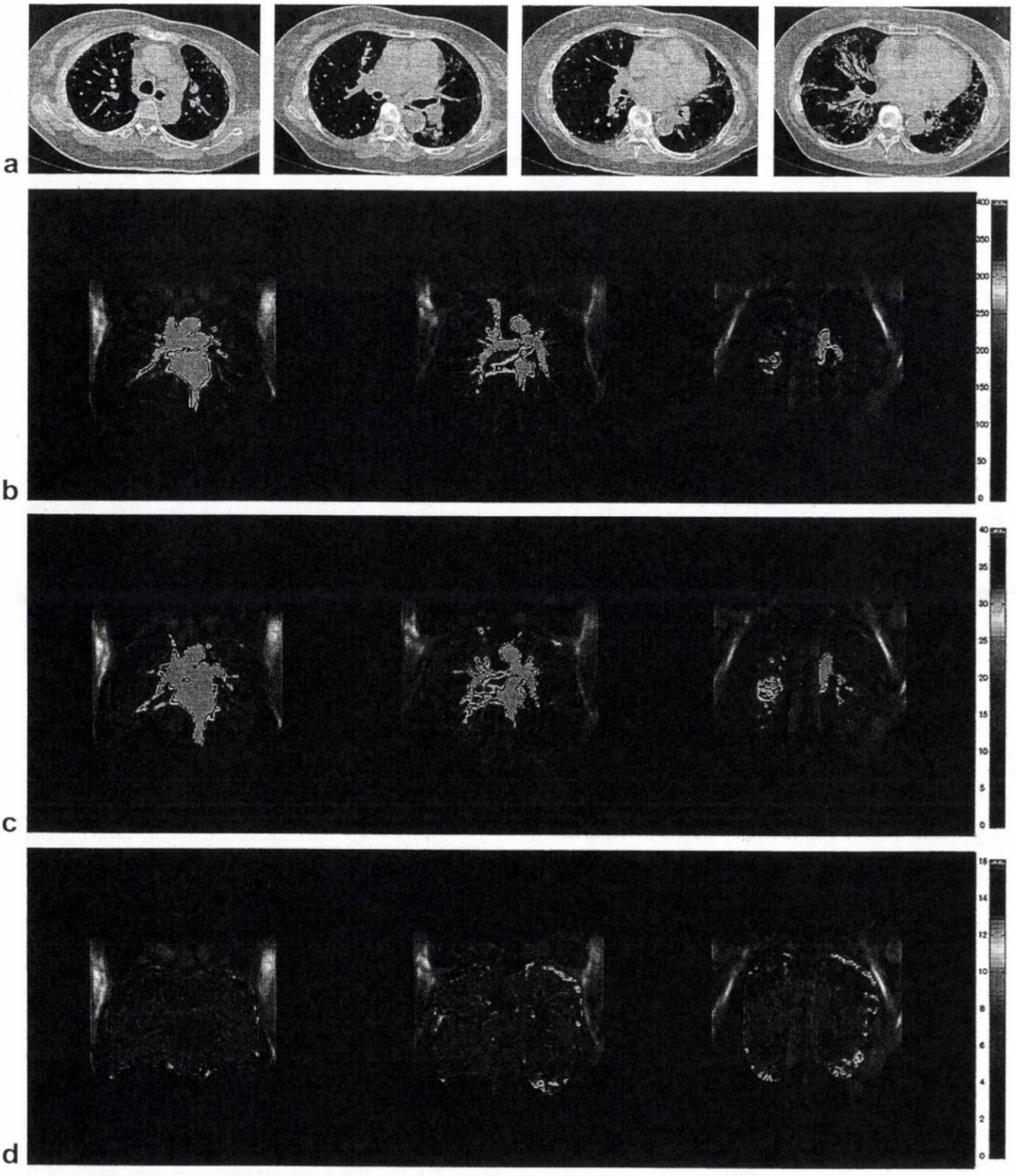

Figure 3. Quantitative pulmonary perfusion parameter maps for a 69-year-old female CTD patient with PAH. **a:** Thin-section CT images (L to R: cranial to caudal) demonstrate ground-glass attenuations, irregular pleural margin, septal and subpleural lines, and subpleural cysts in the both lungs. CT-based disease severity was assessed as 27. **b:** Image maps (L to R: ventral to dorsal) of PBF from coronal 3D dynamic MR data show heterogeneously and markedly reduced regional PBF in the gravitational and isogravitational directions. mPBF was 118.0 ± 34.2/100 mL/min. **c:** Image maps (L to R: ventral to dorsal) of PBV from coronal 3D dynamic MR data show heterogeneously and markedly reduced regional PBV in the gravitational and isogravitational directions. mPBV was 12.5 ± 5.2/100 mL. **d:** Image maps (L to R: ventral to dorsal) of MTT from coronal 3D dynamic MR data show heterogeneously prolonged regional MTT in the gravitational and isogravitational directions. mMTT was 6.4 ± 2.8 seconds.

Table 1
Comparisons of sPAP, FEV_1%, %DLCO, CT-Based Disease Severity, mPBF, mPBV, and mMTT of Healthy Volunteers and CTD Patients With and Without PAH

	Healthy volunteers	CTD patients	
		Without PAH	With PAH
Age (years)	54 ± 9	55 ± 11	59 ± 8
Gender (male:female)	2:07	2:07	2:07
sPAP (mmHg)	21.6 ± 6.6	27.1 ± 6.1	49.7 ± 7.9[a,b]
%FEV_1 (%)	83.4 ± 13.8	80.6 ± 7.5	78.6 ± 10.3
%VC (%)	84.7 ± 5.1	72.1 ± 6.6[a]	67.9 ± 8.7[a]
%DLCO (%)	82.1 ± 8.8	50.1 ± 11.7[a]	40.8 ± 12.1[a]
CT-based disease severity	N/A	5.9 ± 4.4	18.2 ± 7.3[b]
mPBF (ml/100ml/min)	170.3 ± 13.2	149.7 ± 21.5[a]	118.6 ± 17.2[a,b]
mPBV (ml/100ml)	15.1 ± 2.1	14.5 ± 2.0	12.8 ± 1.0[a]
mMTT (sec)	5.3 ± 0.4	5.8 ± 0.4	6.6 ± 0.9[a,b]

CTD, Connective tissue disease; PAH, Pulmonary arterial hypertension; sPAP, Systolic pulmonary arterial pressure; FEV_1%, Percentage predicted forced expiratory volume in 1 second; %DLCO, Percentage predicted diffusing capacity for carbon monoxide; mPBF, Mean of pulmonary blood flow, mPBV, Mean of pulmonary blood volume, mMTT, Mean of mean transit time, N/A, not applicable.
[a]Significant difference with healthy volunteers ($P < 0.05$).
[b]Significant difference with CTD patients without PAH ($P < 0.05$).

where $C_{VOI}(t)$ and $C_{AIF}(t)$ are the time-dependent concentrations of the contrast agent in the VOI and the AIF, respectively. R(t) is the residue function that is the relative amount of contrast agent in the VOI in an idealized perfusion experiment, where a unit area bolus is instantaneously injected [R(0) = 1] and subsequently washed out by perfusion [R(∞) = 0]. It follows from Eq. [1] that the initial height of the deconvolved time–concentration curve equals the PBF.

There are several methods for calculating R(t) from Eq. [1] by deconvolution. In this study we adopted an algebraic approach based on singular value decomposition (SVD), which is robust against statistical noise. The details of this approach have been described elsewhere (31–33). We generated the PBF maps by applying this approach pixel-by-pixel. AIF was obtained from the main trunk of the pulmonary artery by using fuzzy clustering (34).

The pulmonary blood volume (PBV) was obtained with the following formula:

$$PBV = \frac{\int_0^\infty C_{VOI}(t)dt}{\int_0^\infty C_{AIF}(t)dt} \quad [2]$$

From the central volume principle, the mean transit time (MTT) is obtained by the equation:

$$MTT = \frac{PBV}{PBF} \quad [3]$$

The details of data analysis and reproducibility of dynamic contrast-enhanced perfusion MRI have been described in previous reports (16,17,22).

Thin-Section CT Examination

All thin-section CT examinations in CTD patients without and with PAH were obtained with a 16 detector-row CT system (Brilliance 16, Philips). The scans were performed from the lung apex to the diaphragm (16 × 0.75 mm collimation, beam pitch 0.938 mm, 300–350 FOV, 512 × 512 matrix, 140 kV, 120 mAs, gantry rotation 0.75 sec) and reconstructed as 1.5 mm contiguous section thickness slices. Before CT examination, patients practiced their breathing to produce full and consistent inspiration. Then, a noncontrast-enhanced CT examination in each CTD patient was performed during breath-holding at the end of full inspiration.

Pulmonary Function Test

For pulmonary function testing, an automatic spirometer (System 9; Minato Ikagaku, Osaka, Japan) was used in accordance with the American Thoracic Society standards (35,36) to assess forced expiratory volume in 1 second (FEV_1%: percentage predicted), vital capacity (%VC: percentage predicted), and diffusing capacity for carbon monoxide ($\%DL_{CO}$: percentage predicted).

Doppler Echocardiography

All subjects underwent Doppler echocardiography examinations administered by two experienced cardiologists according to the standard technique established by the American Society of Echocardiography (37). The sPAP was estimated based on the modified Bernoulli equation as follows:

$$sPAP = RAP + 4v^2 \quad [4]$$

where RAP is the right arterial pressure and v is the maximum peak of tricuspid regurgitation velocity. All subjects underwent the Doppler echocardiographic examination twice and the two estimated values were averaged for the final sPAP.

Rights-Side Heart Catheterization

A Swan-Ganz catheter (Baxter Healthcare, Irvine, CA) was advanced into the main pulmonary artery of every patient after puncture of the brachial or jugular vein

and mean pulmonary arterial pressure (mPAP), pulmonary capillary wedge pressure (PCWP), cardiac output (CO), and PVR (derived from the difference between mPAP and PCWP divided by CO) were measured by experienced cardiologists. Cardiac output was measured with standard methods for 4 minutes on three to five occasions and the results were averaged.

Image Analysis

Dynamic Contrast-Enhanced Perfusion MRI

To compare the regional PBF, PBV, and MTT of healthy subjects and CTD patients with and without PAH, regions of interests (ROIs) were established by two chest radiologists with 6 and 14 years' experience. These ROIs were located in the right upper, right middle, right lower, left upper, left middle, and left lower lung areas without the large vessels on every slice of calculated quantitative PBF, PBV, and MTT maps. For the purposes of our study, each ROI measured 10 mm in diameter. ROIs in each lung field on every slice were placed twice by each radiologist. Next, the means of PBF (mPBF), PBV (mPBV), and MTT (mMTT) were determined as the average of, respectively, the regional PBF, PBV, and MTT from all ROIs.

Thin-Section CT

To determine the relationship between quantitative pulmonary perfusion parameters and lung structural changes in CTD patients, CT-based disease severity was scored by two independent chest radiologists with 14 and 17 years' experience. According to the past literature (38), visual evaluation included a score of severity and score of extent. The former is based on appreciation of the parenchymal abnormalities assumed to reflect increasing severity of lung involvement: ground-glass opacity (score = 1), irregular pleural margins (score = 2), septal and subpleural lines (score = 3), honeycombing (score = 4), and subpleural cysts (score = 5). The severity score thus ranged from 0 (no abnormality) to 15 (all abnormalities present). The extent score was obtained by counting the numbers of bronchial pulmonary segments in which any of the previous abnormalities are observed: one to three segments involved implied a score of 1; four to nine segments implied a score of 2; more than nine segments implied a score of 3. The extent score thus ranged from 0 (no abnormality in any segment) to 15 (all five abnormalities in more than nine segments). Then, severity and extent of disease scores were added to obtain a total score (range, 0–30). Finally, CT-based disease severity in each CTD patient was determined as the average of total scores independently assessed by two observers.

Statistical Analysis

To determine the difference between healthy volunteers and CTD patients with and without PAH, sPAP, FEV_1%, $\%DL_{CO}$, mPBF, mPBV and mMTT were statistically compared by using the analysis of variance (ANOVA) followed by Fisher's Protected Least Significant Difference (PLSD) tests.

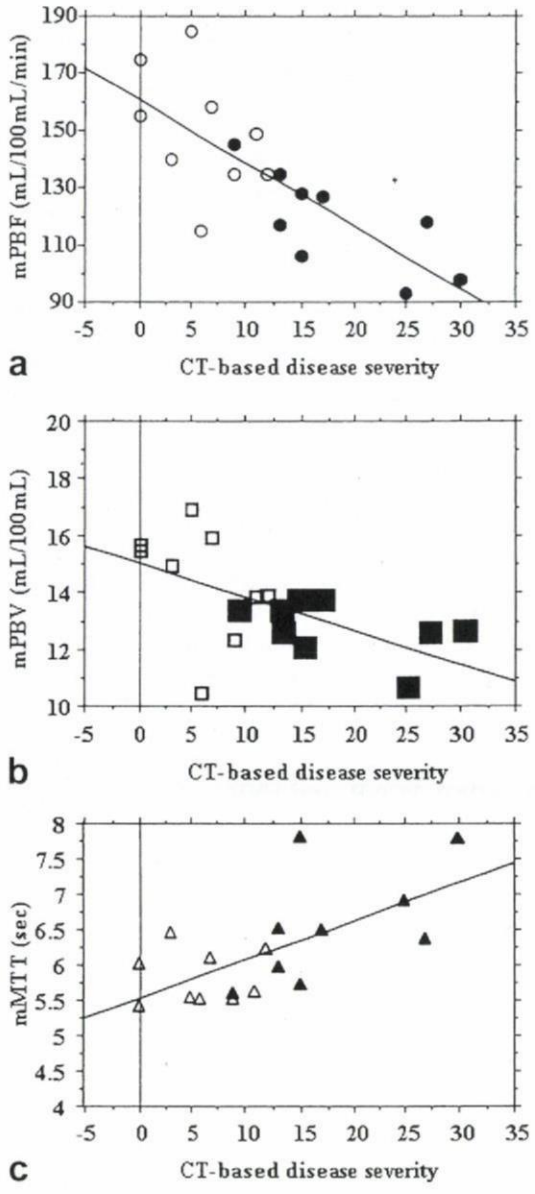

Figure 4. Correlation between CT-based disease severity and means of pulmonary perfusion parameters in CTD patients without and with PAH. **a:** Graph (open circles: CTD patients without PAH, solid circles: CTD patients with PAH) shows the significantly good and negative correlation between CT-based disease severity and mPBF ($r = -0.77$, $P < 0.01$). **b:** Graph (open squares: CTD patients without PAH, solid squares: CTD patients with PAH) shows the significantly moderate and negative correlation between CT-based disease severity and mPBV ($r = -0.59$, $P = 0.01$). **c:** Graph (open triangles: CTD patients without PAH, solid triangles: CTD patients with PAH) shows the significant moderate and positive correlation between CT-based disease severity and mMTT ($r = 0.65$, $P < 0.01$).

To assess the difference of CT-based disease severity in CTD patients, CT-based disease severity was also compared between CTD patients without PAH and that with PAH by using Student's t-test.

To determine the relationship between lung structural changes and pulmonary perfusion parameters in CTD patients, mPBF, mPBV, and mMTT were statistically correlated with CT-based disease severity.

Table 2
Correlations Among CT-Based Disease Severity, Mean Pulmonary Perfusion Parameters, Doppler Echo Cardiographic Index and Pulmonary Functional Parameters for CTD Patients (n = 18) Without and With PAH

	CT-based disease severity	mPBF	mPBV	mMTT
	r (P value)	r (P value)	r (P value)	r (P value)
sPAP	0.71[a] (<0.01)	−0.79[a] (<0.01)	−0.59[a] (<0.01)	0.62[a] (<0.01)
FEV_1%	0.15 (0.55)	0.09 (0.71)	0.13 (0.60)	−0.47 (0.85)
%VC	0.32 (0.19)	0.38 (0.12)	0.20 (0.42)	−0.45 (0.06)
%DLCO	−0.65[a] (<0.01)	0.77[a] (<0.01)	0.61[a] (<0.01)	−0.57[a] (<0.01)

CTD, Connective tissue disease; PAH, Pulmonary arterial hypertension; sPAP, Systolic pulmonary arterial pressure; FEV_1%, Percentage predicted forced expiratory volume in 1 second; %DLCO, Percentage predicted diffusing capacity for carbon monoxide; mPBF, Mean of pulmonary blood flow, mPBV, Mean of pulmonary blood volume, mMTT, Mean of mean transit time
[a]Significant correlation between two parameters ($P < 0.05$).

To evaluate correlations between pulmonary perfusion parameters and the noninvasively assessed disease severity in CTD patients, CT-based disease severity, mPBF, mPBV, and mMTT were statistically correlated with sPAP, FEV_1%, %VC, and $\%DL_{CO}$.

Moreover, to determine correlations between pulmonary perfusion parameters and invasive hemodynamic parameters from right heart catheterization in CTD patients with PAH patients, CT-based disease severity, mPBF, mPBV, and mMTT were statistically correlated with CO, mPAP, PCWP, and PVR.

A *P*-value of less than 0.05 was considered significant in all statistical analyses.

RESULTS

All 3D dynamic perfusion MRIs were successfully completed without any adverse effects. Representative cases of a healthy volunteer and CTD patients with and without PAH are shown in Figs. 1–3.

Results of comparison of sPAP, FEV_1%, $\%DL_{CO}$, mPBF, mPBV, and mMTT among healthy volunteers and CTD patients with and without PAH and comparison of CT-based disease severity in CTD patients are shown in Table 1. A comparison of healthy volunteers and CTD patients without and with PAH showed that %VC, $\%DL_{CO}$, and mPBF of the former were significantly higher ($P < 0.05$). Moreover, mPBV of healthy volunteers was significantly higher than that of CTD patients with PAH ($P < 0.05$), and their sPAP was significantly lower than that of CTD patients with PAH ($P < 0.05$). The mMTT of healthy volunteers was also significantly shorter than that of CTD patients with PAH ($P < 0.05$). A comparison of CTD patients without and with PAH showed that sPAP and mPBF of the former were significantly higher ($P < 0.05$), and their mMTT was significantly shorter ($P < 0.05$). In addition, CT-based disease severity of CTD patients with PAH was significantly higher than that of CTD patients without PAH ($P < 0.05$).

The results of correlation between CT-based disease severity and means of pulmonary perfusion parameters are shown in Fig. 4. CT-based disease severity had significantly good and negative correlation with mPBF ($r^2 = 0.59$, $P < 0.01$), and significantly moderate and negative correlation with mPBV ($r^2 = 0.35$, $P = 0.01$). In addition, CT-based disease severity had significantly moderate and positive correlation with mMTT ($r^2 = 0.42$, $P < 0.01$).

Results of correlation among CT-based disease severity, pulmonary perfusion parameters, Doppler echo cardiographic index, and pulmonary functional parameters for all CTD patients are shown in Table 2. CT-based disease severity and mean pulmonary perfusion parameters as having significant correlation with Doppler echo cardiographic index and pulmonary functional parameters are also shown in Figs. 5 and 6. CT-based disease severity correlated significantly with sPAP ($r^2 = 0.50$, $P < 0.01$) and $\%DL_{CO}$ ($r^2 = 0.42$, $P < 0.01$), mPBF with sPAP ($r^2 = 0.62$, $P < 0.01$) and $\%DL_{CO}$ ($r^2 = 0.59$, $P < 0.01$), mPBV with sPAP ($r^2 = 0.35$, $P < 0.01$) and $\%DL_{CO}$ ($r^2 = 0.37$, $P < 0.01$), and mMTT with sPAP ($r^2 = 0.38$, $P < 0.01$) and $\%DL_{CO}$ ($r^2 = 0.32$, $P < 0.01$).

Results of correlation among CT-based disease severity, pulmonary perfusion parameters, and invasive hemodynamic parameters in CTD patients with PAH are shown in Table 3. Mean pulmonary perfusion parameters as having significant correlation with invasive hemodynamic parameters are also shown in Figs. 7 and 8. mPBF and mPBV significantly correlated with mPAP (mPBF: $r^2 = 0.49$, $P = 0.04$; mPBV: $r^2 = 0.50$, $P = 0.03$), and PVR (mPBF: $r^2 = 0.55$, $P = 0.03$; and mPBV: $r^2 = 0.61$, $P = 0.01$).

DISCUSSION

Our results show that 3D dynamic contrast-enhanced perfusion MRI combined with the indicator dilution technique can quantitatively assess pulmonary perfusion abnormalities and disease severity in CTD patients with and without PAH. To the best of our knowledge, ours is the first reported study to use 3D dynamic contrast-enhanced perfusion MRI for the noninvasive assessment of disease severity in CTD patients in order to quantitatively determine changes in pulmonary perfusion parameters due to underlying pathophysiology. In addition, this procedure was used to analyze the relationship between quantitatively analyzed pulmonary perfusion parameter changes and the findings of Doppler echocardiography, the pulmonary function test, and right heart catheterization studies.

Two types of lung disease have been identified in systemic sclerosis and MCTD: pulmonary interstitial

fibrosis and PAH (1–5). As a result of inflammation and fibrosis affecting the alveolar walls, the following abnormalities are frequently observed: 1) diminished compliance of the lung, 2) an overall reduction in lung volume, 3) impairment of diffusion, 4) abnormalities in small airways function without generalized airflow obstruction, 5) disturbances in gas exchange, and 6) in some cases pulmonary hypertension (39). In addition, findings of previous histological examinations of CTD patients with systemic sclerosis and/or MCTD patients suggest that endothelial injury and dysfunction of small pulmonary arteries and arterioles may lead to vascular remodeling and vasospasm (1,40–42). These abnormalities also cause a variety of anatomical changes such as isolated medial hypertrophy, migration of muscle cells into smaller vessels, intimal proliferation, plexiform arteriopathy, and fibrinoid necrosis in PAH (41,43). Therefore, significant differences of %VC, $\%DL_{CO}$, and pulmonary perfusion parameters among healthy volunteers and CTD patients without and with PAH may be considered as resulting from the aforementioned pathological and physiopathological abnormalities in the lung.

In addition, pulmonary hypertension and cor pulmonale often develop in patients with severe CTD. The cause of pulmonary hypertension is rarely a primary process affecting pulmonary vessels as well as alveolar walls, but more frequently a process occurring in the alveolar walls. There are two main factors contributing to this process: 1) hypoxia and 2) obliteration of small pulmonary vessels by the fibrotic process in the alveolar walls (39–42). In addition, a reduction in the pulmonary vascular bed due to pulmonary in situ thrombosis or thromboembolism as well as the previously mentioned pathological changes may be involved in PAH associated with CTD patients (39–42). Therefore, the significant differences in sPAP, mPBF, mPBV, and mMTT between healthy volunteers and CTD patients with PAH established in our study can be considered compatible with these reported physiopathologic and pathologic features of CTD patients with PAH. The same holds true for the differences in sPAP, mPBF, and mMTT between CTD patients without and with PAH.

Moreover, our results of comparison of CT-based disease severity in CTD patients and correlations between CT-based disease severity and quantitative pulmonary perfusion parameters suggest that lung structural changes can assess disease severity in CTD patients and significantly affected regional changes of pulmonary perfusion parameters. CT-based disease severity on thin-section CT is suggested to play an important role for disease severity assessment and management in patients with systemic sclerosis (38). Therefore, pulmonary perfusion parameters may have the potential to

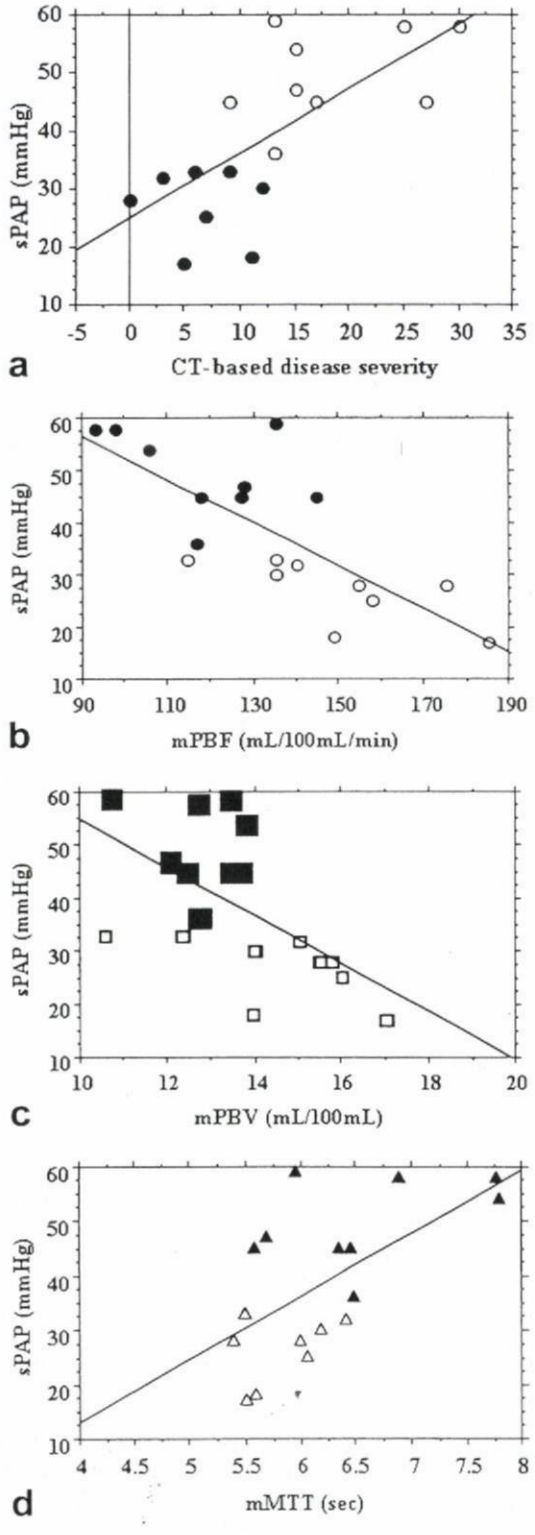

Figure 5. Correlation among CT-based disease severity, means of pulmonary perfusion parameter, and sPAP in CTD patients without and with PAH. **a:** Graph (solid circles: CTD patients without PAH, open circles: CTD patients with PAH) shows the significantly good and positive correlation between CT-based disease severity and sPAP ($r = 0.71$, $P < 0.01$). **b:** Graph (open circles: CTD patients without PAH, solid circles: CTD patients with PAH) shows the significantly good and negative correlation between mPBF and sPAP ($r = -0.79$, $P < 0.01$). **c:** Graph (open squares: CTD patients without PAH, solid squares: CTD patients with PAH) shows the significantly moderate and negative correlation between mPBV and sPAP ($r = -0.59$, $P < 0.01$). **d:** Graph (open triangles: CTD patients without PAH, solid triangles: CTD patients with PAH) shows the significantly moderate and positive correlation between mMTT and sPAP ($r = -0.62$, $P < 0.01$).

assess disease severity and adapt for management of CTD patients as well as CT-based disease severity on thin-section CT.

Analysis of the relationships among CT-based disease severity, quantitatively assessed pulmonary perfusion MR, Doppler echo cardiographic, and pulmonary functional parameters for all CTD patients, CT-based disease severity, and quantitative pulmonary perfusion parameters showed significant correlations with sPAP and $\%DL_{CO}$. CT-based disease severity and Doppler echo cardiographic and pulmonary functional parameters are thought to be predictors of disease severity and/or progression of PAH in CTD patients to such complications as systemic sclerosis and/or MCTD (1,38–42). Our results therefore suggest that quantitatively assessed pulmonary perfusion parameters may be useful for assessment of disease severity and/or progression of PAH in CTD patients as well as CT-based disease severity on thin-section CT.

The findings of the aforementioned pathologic and physiopathologic analyses and the hemodynamic analysis of pulmonary circulation suggest that mPAP and PVR may function as predictors of disease severity in CTD patients with PAH as well as primary PAH (1,39–42). When analyzed, the relationship between quantitatively assessed perfusion MRI and right heart catheterization, quantitative pulmonary perfusion parameters, except for mMTT, either significantly or moderately correlate with mPAP and PVR. In addition, there were no significant correlation between CT-based disease severity and the above-mentioned predictors in CTD patients with PAH.

PVR is generally defined as follows:

$$PVR = (mPAP - PCWP)/CO \cong (mPAP - PCWP)/PBF \quad [5]$$

This means that PBF is directly affected by mPAP and PVR, and may significantly correlate with these two parameters. In addition, pulmonary in situ thrombosis and/or thromboembolism causes a reduction in the pulmonary capillary bed and pulmonary blood volume. Therefore, mPBV as well as mPBF may correlate with mPAP and PVR, which is also compatible with quantitatively assessed contrast-enhanced perfusion MR parameters and pulmonary hemodynamic parameters assessed by right heart catheterization in PAH patients as reported in the literature (18). In contrast to PBF and PBV, which were directly calculated from the signal–intensity time course curve of 3D dynamic contrast-enhanced perfusion MR data, MTT was determined with Eq. [3], which is based on indicator dilution theory, and is considered to reflect the calculated PBF and PBV. Therefore, the fact that no significant correla-

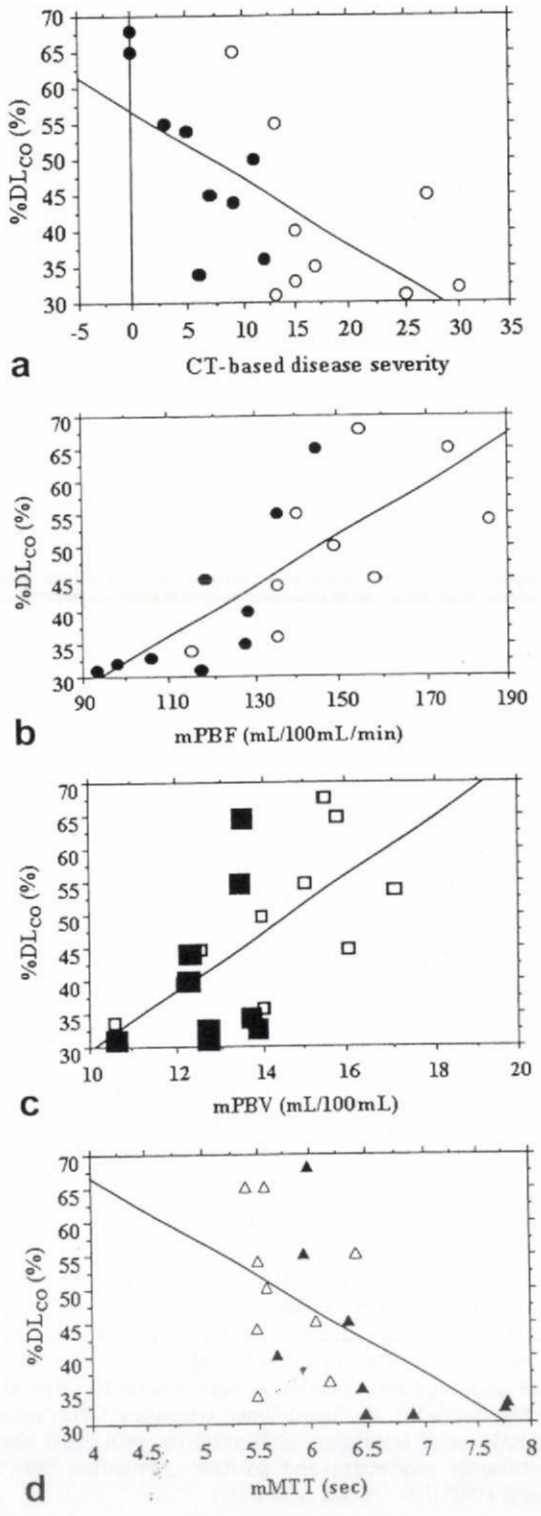

Figure 6. Correlation among CT-based disease severity, means of pulmonary perfusion parameter, and $\%DL_{CO}$ in CTD patients without and with PAH. **a:** Graph (solid circles: CTD patients without PAH, open circles: CTD patients with PAH) shows the significantly good and negative correlation between CT-based disease severity and $\%DL_{CO}$ ($r = -0.65$, $P < 0.01$). **b:** Graph (open circles: CTD patients without PAH, solid circles: CTD patients with PAH) shows the significantly good and positive correlation between mPBF and $\%DL_{CO}$ ($r = 0.77$, $P < 0.01$). **c:** Graph (open squares: CTD patients without PAH, solid squares: CTD patients with PAH) shows the significantly moderate and positive correlation between mPBV and $\%DL_{CO}$ ($r = 0.61$, $P < 0.01$). **d:** Graph (open triangles: CTD patients without PAH, solid triangles: CTD patients with PAH) shows the significantly moderate and negative correlation between mMTT and $\%DL_{CO}$ ($r = -0.57$, $P < 0.01$).

Table 3
Comparison Among CT-Based Disease Severity, Quantitative Pulmonary Perfusion Parameters and Right Heart Catheterization Parameters of CTD Patients (n = 9) With PAH

	CT-based disease severity	mPBF	mPBV	mMTT
	r (*P* value)	*r* (*P* value)	*r* (*P* value)	*r* (*P* value)
CO	−0.32 (0.40)	0.29 (0.46)	0.38 (0.32)	−0.18 (0.64)
mPAP	0.44 (0.24)	−0.70[a] (0.04)	−0.71[a] (0.03)	0.37 (0.33)
PCWP	0.13 (0.75)	−0.20 (0.61)	−0.36 (0.34)	0.09 (0.83)
PVR	0.60 (0.69)	−0.74[a] (0.02)	−0.78[a] (0.01)	0.42 (0.26)

CTD, Connective tissue disease; PAH, Pulmonary arterial hypertension; CO, Cardiac output; mPAP, Mean pulmonary arterial pressure; PCWP, Pulmonary capillary wedge pressure; PVR, Pulmonary vascular resistance; mPBF, Mean of pulmonary blood flow, mPBV, Mean of pulmonary blood volume, mMTT, Mean of mean transit time
[a]Significant correlation between two parameters ($P < 0.05$).

tion between mMTT and pulmonary hemodynamic parameters was found in our study seems to suggest that mPBF and mPBV may be more sensitive and less affected parameters than mMTT for the assessment of disease severity as indicated by PVR and mPAP in CTD patients with PAH. In addition, quantitatively assessed dynamic perfusion MRI may have better potential for noninvasive assessment of disease severity as indicated by PVR and mPAP in CTD patients with PAH.

There are a few limitations to our study. First, while all dynamic perfusion MRI examinations were successfully completed without adverse effects, and we were able to complete all calculations of regional perfusion from the signal intensity–time course curves, two CTD patients without PAH and four with PAH needed to "shallow-breathing" for data acquisition so that the image quality was slightly degraded between 16.5 and 22 seconds after bolus injection of contrast media. Severe CTD patients without and with PAH whose pulmonary function is low may result in under- or overestimation of regional perfusion and regional pulmonary function due to motion misregistration artifact. However, 3D dynamic perfusion MRI is still a new technique for assessment of quantitative regional pulmonary perfusion, and development of faster scanning time and new phase encoding schemes for reduction of motion artifact may make this technique more practical.

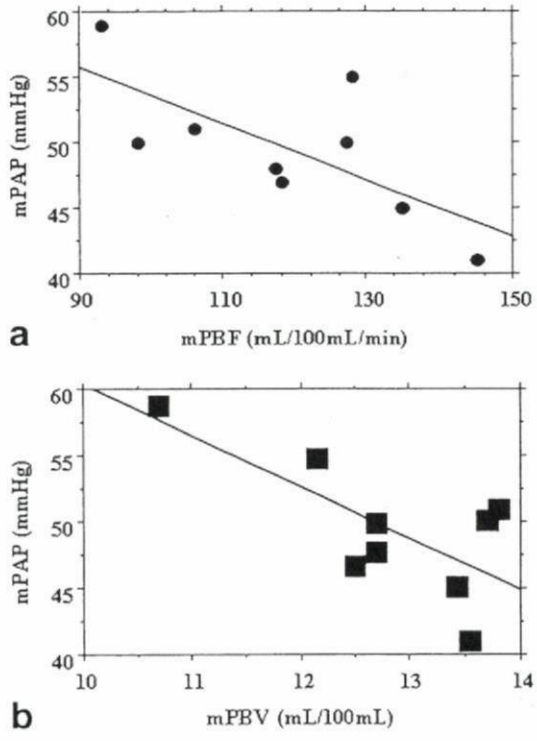

Figure 7. Correlation between means of pulmonary perfusion parameter and mPAP in CTD patients with PAH. **a:** Graph shows the significantly good and negative correlation between mPBF and mPAP ($r = -0.70$, $P = 0.04$). **b:** Graph shows the significantly good and negative correlation between mPBV and mPAP ($r = -0.71$, $P = 0.03$).

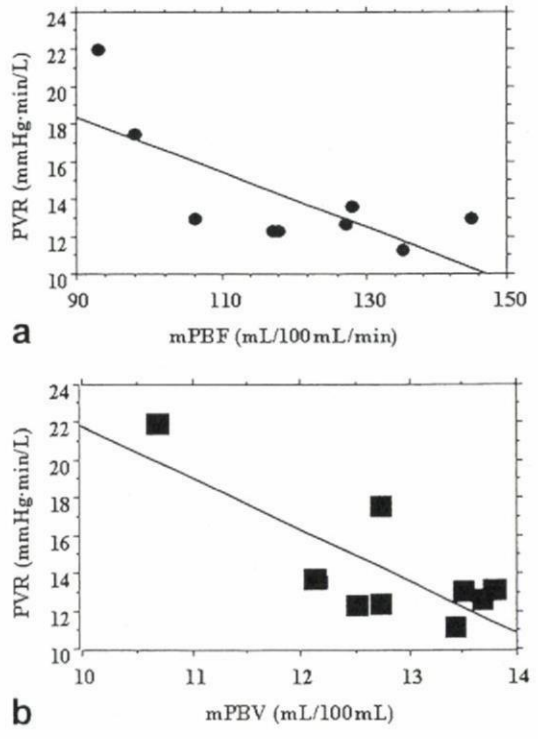

Figure 8. Correlation between means of pulmonary perfusion parameter and PVR in CTD patients with PAH. a: Graph shows the significantly good and negative correlation between mPBF and PVR ($r = -0.74$, $P = 0.02$). b: Graph shows the significantly good and negative correlation between mPBV and PVR ($r = -0.78$, $P = 0.01$).

Second, although we examined number-, gender-, and age-matched nonsmoking healthy volunteers and CTD patients selected from an initially examined 72 CTD patients without and with PAH in this study, the size of our number-, gender-, and age-matched study population was small because the numbers of CTD patients with PAH were only nine. Therefore, to demonstrate the real significance of 3D dynamic perfusion MRI for noninvasive assessment of disease severity of CTD patients and for evaluation of the severity of PAH, a large prospective trial should be performed as a further investigation in the near future.

Third, we compared or correlated averaged pulmonary perfusion parameters from multiple ROI measurements with parameters measured by pulmonary function test, cardiac echogram, and right heart catheterization, although we tried to demonstrate the utility of 3D dynamic contrast-enhanced MR imaging for assessment of disease severity and/or progression of PAH in small numbers of CTD patients. In addition, we evaluated each subject once in this study, and could not assess disease progression because we did not perform dynamic perfusion MR examination in each subject at several timepoints. Moreover, we did not directly compare regional pulmonary perfusion parameter changes with regional lung structure changes, although we compared capability for disease severity assessment between means of pulmonary perfusion parameters and CT-based disease severity as well as correlation between means of pulmonary perfusion parameters and CT-based disease severity in CTD patients without and with PAH. Furthermore, changes in the perfusion parameters could not be compared in terms of 3D dynamic perfusion MRI, other MR techniques or analyses, and nuclear medicine methods such as SPECT and PET in this study. Therefore, to demonstrate the real significance of 3D dynamic perfusion MRI for noninvasive assessment of disease severity and/or progression of CTD patients and for evaluation of disease severity and/or progression of PAH, a large prospective trial using quantitatively analyzed regional pulmonary perfusion parameters is needed for a comparison of 3D dynamic perfusion MRI, other MR techniques or analyses, nuclear medicine techniques, and quantitatively and qualitatively assessed lung structure changes on thin-section CT as well as parameters obtained by cardiac echogram, pulmonary perfusion test, and right heart catheterization at several times in near future.

In conclusion, quantitatively assessed 3D dynamic perfusion MRI has the potential for assessment of disease severity and progression of PAH in CTD patients. Moreover, this technique, similar to Doppler echocardiography and the pulmonary function test, may help noninvasive physiopathological assessment of CTD patients, and may be used as a substitute for right heart catheterization for CTD patients with PAH.

ACKNOWLEDGMENTS

The authors thank Kazuyuki Kobayashi, MD, PhD, Yasuhiro Funada, MD, PhD, Tetuari Onishi, MD, Yoshikazu Kotani, MD, Yoshihiro Nishimura, MD, Noriaki Emoto, MD, PhD, Hiroya Kawai, MD (Division of Cardiovascular and Respiratory Medicine, Department of Internal Medicine, Kobe University Graduate School of Medicine); Tomoko Nakamura, MD, Shin-ichi Kumagai, MD (Department of Laboratory Medicine, Graduate School of Medicine, Kobe University); Takeshi Yoshikawa, MD, PhD (Department of Radiology, Kohnan Hospital); and Hideaki Kawamitsu, BS (Division of Radiology, Kobe University Hospital) for contributions to this study.

REFERENCES

1. Hoeper MM. Pulmonary hypertension in collagen vascular disease. Eur Respir J 2002;19:571–576.
2. Yamane K, Ihn H, Asano Y, et al. Clinical and laboratory features of scleroderma patients with pulmonary hypertension. Rheumatology 2000;39:1269–1271.
3. Murata I, Takenaka K, Yoshinoya S, et al. Clinical evaluation of pulmonary hypertension in systemic sclerosis and related disorders. A Doppler echocardiographic study of 135 Japanese patients. Chest 1997;111:36–43.
4. Hoffman RW, Greidinger EL. Mixed connective tissue disease. Curr Opin Rheumatol 2000;12:386–390.
5. Yousem SA. The pulmonary pathologic manifestations of the CREST syndrome. Hum Pathol 1990;21:467–474.
6. Edwards PD, Bull RK, Coulden R. CT measurement of main pulmonary artery diameter. Br J Radiol 1998;71:1018–1020.
7. Haimovici JB, Trotman-Dickenson B, Halpern EF, et al. Relationship between pulmonary artery diameter at computed tomography and pulmonary artery pressures at right-sided heart catheterization. Massachusetts General Hospital Lung Transplantation Program. Acad Radiol 1997;4:327–334.
8. Mousseaux E, Tasu JP, Jolivet O, Simonneau G, Bittoun J, Gaux JC. Pulmonary arterial resistance: noninvasive measurement with indexes of pulmonary flow estimated at velocity-encoded MR imaging—preliminary experience. Radiology 1999;212:896–902.
9. Laffon E, Laurent F, Bernard V, De Boucaud L, Ducassou D, Marthan R. Noninvasive assessment of pulmonary arterial hypertension by MR phase-mapping method. J Appl Physiol 2001;90:2197–2202.
10. Worsley DF, Palevsky HI, Alavi A. Ventilation-perfusion lung scanning in the evaluation of pulmonary hypertension. J Nucl Med 1994;35:793–796.
11. Fukuchi K, Hayashida K, Nakanishi N, et al. Quantitative analysis of lung perfusion in patients with primary pulmonary hypertension. J Nucl Med 2002;43:757–761.
12. Ohno Y, Hatabu H, Takenaka D, Adachi S, Hirota S, Sugimura K. Contrast-enhanced MR perfusion imaging and MR angiography: utility for management of pulmonary arteriovenous malformations for embolotherapy. Eur J Radiol 2002;41:136–146.
13. Ohno Y, Hatabu H, Takenaka D, Adachi S, Kono M, Sugimura K. Solitary pulmonary nodules: potential role of dynamic MR imaging in management initial experience. Radiology 2002;224:503–511.
14. Ohno Y, Nogami M, Higashino T, et al. Prognostic value of dynamic MR imaging for non-small-cell lung cancer patients after chemoradiotherapy. J Magn Reson Imaging 2005;21:775–783.
15. Ohno Y, Hatabu H, Higashino T, et al. Dynamic perfusion MRI versus perfusion scintigraphy: prediction of postoperative lung function in patients with lung cancer. Am J Roentgenol 2004;182:73–78.
16. Ohno Y, Hatabu H, Murase K, et al. Quantitative assessment of regional pulmonary perfusion in the entire lung using three-dimensional ultrafast dynamic contrast-enhanced magnetic resonance imaging: preliminary experience in 40 subjects. J Magn Reson Imaging 2004;20:353–365.
17. Ohno Y, Hatabu H, Murase K, et al. Primary pulmonary hypertension: 3D dynamic perfusion MRI for quantitative analysis of regional pulmonary perfusion. Am J Roentgenol 2007;188:48–56.
18. Ley S, Mereles D, Risse F, et al. Quantitative 3D pulmonary MR-perfusion in patients with pulmonary arterial hypertension: correlation with invasive pressure measurements. Eur J Radiol 2007;61:251–255.
19. Ohno Y, Koyama H, Nogami M, et al. Postoperative lung function in lung cancer patients: comparative analysis of predictive capability of MRI, CT, and SPECT. Am J Roentgenol 2007;189:400–408.

20. Nikolaou K, Schoenberg SO, Brix G, et al. Quantification of pulmonary blood flow and volume in healthy volunteers by dynamic contrast-enhanced magnetic resonance imaging using a parallel imaging technique. Invest Radiol 2004;39:537–545.
21. Fink C, Puderbach M, Ley S, et al. Contrast-enhanced three-dimensional pulmonary perfusion magnetic resonance imaging: intraindividual comparison of 1.0 M gadobutrol and 0.5 M Gd-DTPA at three dose levels. Invest Radiol 2004;39:143–148.
22. Ohno Y, Murase K, Higashino T, et al. Assessment of bolus injection protocol with appropriate concentration for quantitative assessment of pulmonary perfusion by dynamic contrast-enhanced MR imaging. J Magn Reson Imaging 2007;25:55–65.
23. Barst RJ, McGoon M, Torbicki A, et al. Diagnosis and differential assessment of pulmonary arterial hypertension. J Am Coll Cardiol 2004;43:S40–S47.
24. Rubin LJ; American College of Chest Physicians. Diagnosis and management of pulmonary arterial hypertension: ACCP evidence-based clinical practice guidelines. Chest 2004;126:S4–6.
25. [No authors listed.] Preliminary criteria for the classification of systemic sclerosis (scleroderma). Subcommittee for Scleroderma Criteria of the American Rheumatism Association Diagnostic and Therapeutic Criteria Committee. Arthritis Rheum 1980;23:581–590.
26. LeRoy EC, Black C, Fleischmajer R, et al. Scleroderma (systemic sclerosis): classification, subsets and pathogenesis. J Rheumatol 1988;15:202–205.
27. Wollheim FA. Classification of systemic sclerosis. Visions and reality. Rheumatology 2005;44:1212–1216.
28. Kasukawa R. Mixed connective tissue disease. Intern Med 1999; 38:386–393.
29. Walker JG, Pope J, Baron M, et al. The development of systemic sclerosis classification criteria. Clin Rheumatol 2007;26:1401–1409.
30. Meier P, Zierler KL. On the theory of the indicator-dilution method for measurement of blood flow and volume. J Appl Physiol 1954;6: 731–744.
31. Ostergaard L, Weisskoff RM, Chesler DA, Gyldensted C, Rosen BR. High resolution measurement of cerebral blood flow using intravascular tracer bolus passages. Part I: Mathematical approach and statistical analysis. Magn Reson Med 1996;36:715–725.
32. Ostergaard L, Sorensen AG, Kwong KK, Weisskoff RM, Gyldensted C, Rosen BR. High resolution measurement of cerebral blood flow using intravascular tracer bolus passages. Part II: Experimental comparison and preliminary results. Magn Reson Med 1996;36: 726–736.
33. Murase K, Shinohara M, Yamazaki Y. Accuracy of deconvolution analysis based on singular value decomposition for quantification of cerebral blood flow using dynamic susceptibility contrast-enhanced magnetic resonance imaging. Phys Med Biol 2001;46:3147–3159.
34. Murase K, Kikuchi K, Miki H, Shimizu T, Ikezoe J. Determination of arterial input function using fuzzy clustering for quantification of cerebral blood flow with dynamic susceptibility contrast-enhanced MR imaging. J Magn Reson Imaging 2001;13:797–806.
35. American Thoracic Society. Standardization of spirometry—1987 update. Am Rev Respir Dis 1987;136:1285–1298.
36. American Thoracic Society. Lung function testing: selection of reference values and interpretative strategies. Am Rev Respir Dis 1991;144:1202–1218.
37. Quinones MA, Otto CM, Stoddard M, Waggoner A, Zoghbi WA; Doppler Quantification Task Force of the Nomenclature and Standards Committee of the American Society of Echocardiography. Recommendations for quantification of Doppler echocardiography: a report from the Doppler Quantification Task Force of the Nomenclature and Standards Committee of the American Society of Echocardiography. J Am Soc Echocardiogr 2002;15:167–184.
38. Camiciottoli G, Orlandi I, Bartolucci M, et al. Lung CT densitometry in systemic sclerosis: correlation with lung function, exercise testing, and quality of life. Chest 2007;131:672–681.
39. Weinberger SE. Overview of the interstitial lung disease. In: Weinberger SE, ed. Principles of pulmonary medicine, 3rd ed. Philadelphia: W.B. Saunders; 1998. p 130–140.
40. Weinberger SE. Pulmonary hypertension. In: Weinberger SE, ed. Principles of pulmonary medicine, 3rd ed. Philadelphia: W.B. Saunders; 1998. p 184–193.
41. Magliano M, Isenberg DA, Hillson J. Pulmonary hypertension in autoimmune rheumatic diseases: where are we now? Arthritis Rheum 2002;46:1997–2009.
42. Proudman SM, Stevens WM, Sahhar J, Celermajer D. Pulmonary arterial hypertension in systemic sclerosis: the need for early detection and treatment. Intern Med J 2007;37:485–494.
43. Heath D, Edwards JE. The pathology of hypertensive pulmonary vascular disease; a description of six grades of structural changes in the pulmonary arteries with special reference to congenital cardiac septal defects. Circulation 1958;18:533–547.

Original Research

Dynamic MRI, Dynamic Multidetector-Row Computed Tomography (MDCT), and Coregistered 2-[fluorine-18]-fluoro-2-deoxy-D-glucose–Positron Emission Tomography (FDG-PET)/CT: Comparative Study of Capability for Management of Pulmonary Nodules

Yoshiharu Ohno, MD, PhD,[1]* Hisanobu Koyama, MD,[1] Daisuke Takenaka, MD,[1] Munenobu Nogami, MD, PhD,[1,2] Yoshimasa Maniwa, MD,[3] Yoshihiro Nishimura, MD,[4] Chiho Ohbayashi, MD,[5] and Kazuro Sugimura, MD[1]

Purpose: To compare the nodule management capabilities of dynamic MRI, dynamic multidetector-row computed tomography (MDCT) and coregistered positron emission tomography (PET)/CT.

Materials and Methods: Dynamic MRI, dynamic MDCT, PET, microbacterial, and pathological examinations were administered to 175 consecutive patients with 202 nodules (<30 mm in diameter). The final diagnoses resulted in the classification of 202 nodules into two groups: requiring further intervention and treatment ($N = 163$) and no further evaluation ($N = 39$) groups. Maximum relative enhancement and slope of enhancement ratio were calculated as dynamic MR indices. Maximum enhancement, net enhancement, slope of enhancement, and absolute loss of enhancement were calculated as dynamic CT indices. maximum value of standard uptake value (SUV_{max}) was measured on coregistered PET/CT. Receiver operating characteristics (ROC) analyses were performed to determine feasible threshold values for nodule management, and results were tested using McNemar's test.

Results: When feasibility threshold values were adopted for nodule management, the specificity (82.1%) and accuracy (93.6%) of the slope of the enhancement ratio were significantly higher than those of dynamic CT indices ($P < 0.05$) and SUV_{max} ($P < 0.05$).

Conclusion: Dynamic MRI can play a more specific and/or accurate role for nodule management as compared with dynamic MDCT and coregistered PET/CT.

Key Words: lung; nodule; MR; CT; PET
J. Magn. Reson. Imaging 2008;27:1284–1295.

THE CHALLENGE OF DIAGNOSIS and management of pulmonary nodules is among the most common and most important areas of pulmonary medicine because pulmonary nodules are caused by a variety of conditions, ranging from benign granulomas to operable primary malignant lung nodules (1–3). Ideally, the goal of diagnosis and management is to promptly bring to surgery all patients with operable malignant nodules while avoiding unnecessary thoracotomy for patients with benign lesions. Therefore, it is important to differentiate malignant from benign nodules in the least invasive manner and to make as specific and accurate a diagnosis as possible (4–21).

Morphologic assessment is helpful for differentiation of malignant from benign nodules, when they show the typical features of benign or malignant nodules. However, in some cases there is considerable overlap between the morphological features of the two types of nodules (1–3,15,16). For more accurate differentiation, some investigators have therefore turned to assessment

[1]Department of Radiology, Kobe University Graduate School of Medicine, Kobe, Japan.
[2]Department of Image-Based Medicine, Institute of Biomedical Research and Innovation, Kobe, Japan.
[3]Division of Cardiovascular, Thoracic, and Pediatric Surgery, Kobe University Graduate School of Medicine, Kobe, Japan.
[4]Division of Cardiovascular and Respiratory Medicine, Department of Internal Medicine, Kobe University Graduate School of Medicine, Kobe, Japan.
[5]Division of Pathology, Kobe University Hospital, Kobe, Japan.
*Address reprint requests to: Y.O., MD, PhD, Department of Radiology, Kobe University Graduate School of Medicine, 7-5-2 Kusunoki-cho, Chuo-ku, Kobe, Hyogo, 650-0017, Japan. E-mail: yosirad@kobe-u.ac.jp; yosirad@med.kobe-u.ac.jp; yoshiharuohno@aol.com
Contract grant sponsor: Knowledge Cluster Initiative of the Ministry of Education, Culture, Sports, Science and Technology of Japan; Contract grant sponsor: Philips Medical Systems; Contract grant sponsor: Schering AG; Contract grant sponsor: Bayer Health Care.
Received July 23, 2007; Accepted February 1, 2008.
DOI 10.1002/jmri.21348
Published online in Wiley InterScience (www.interscience.wiley.com).

of the blood flow patterns of malignant and benign pulmonary nodules by using dynamic computed tomography (CT) and dynamic magnetic resonance imaging (MRI) with conventional and/or fast spin- or gradient-echo sequences (4–9, 17–21). They have also evaluated their glucose metabolism by means of positron emission tomography (PET) with 2-[fluorine-18]-fluoro-2-deoxy-D-glucose (FDG) (4–14,17–21). Although some promising results have been reported for dynamic CT, dynamic MRI, and PET, a substantial portion of nodules remain radiographically too vague for an accurate diagnosis. This is because some malignant nodules with relatively lower malignant potential may yield false-negative results and some active infectious nodules or organizing pneumonia with high blood supply or glucose metabolism may yield false-positive results (4–14,17–21).

Recent technological advances in the form of multidetector-row CT (MDCT) and ultrafast gradient-echo sequencing for dynamic contrast-enhanced perfusion MRI allow for more accurate evaluation of hemodynamics as compared to that attainable with single-helical CT or conventional spin-echo, turbo spin-echo, or gradient-echo sequences on MRI. Jeong et al (8) used dynamic CT with an MDCT system and reported high diagnostic capability as evaluated in terms of combined net enhancement with wash-out patterns in the delayed dynamic phase. Furthermore, the use of an ultrafast dynamic MRI base for dynamic perfusion MRI reported high diagnostic capability for distinguishing malignant from benign pulmonary nodules and seems to have the potential for playing an important role in the management of pulmonary nodules (18–20). Furthermore, recent advances in PET and CT image fusion techniques (coregistered PET/CT or indirect PET/CT) or development of a PET/CT scanner (direct PET/CT) can be expected to improve assessment of tissue glucose metabolism in oncologic patients by using the standard uptake value (SUV) (9,14). However, to our knowledge, no comparative studies have been conducted of the diagnostic capabilities of dynamic MDCT, dynamic MRI based on the dynamic perfusion MR technique, and direct or indirect PET/CT for differentiation of malignant from benign pulmonary nodules and pulmonary nodule management.

We hypothesized that dynamic MRI based on the dynamic perfusion MR technique can more accurately characterize pulmonary nodules than can dynamic MDCT or PET/CT. The purpose of our study was therefore to compare the nodule management capabilities of dynamic MRI, dynamic MDCT, and coregistered PET/CT.

MATERIALS AND METHODS

Subjects

Our institutional review board approved the study, and written informed consent was obtained from all patients.

A total of 175 consecutive patients (92 males, 83 females; mean age = 72.1 years; age range = 36–85 years) with 202 pulmonary nodules (mean diameter = 15.7 ± 5.9 mm, mean ± standard deviation [SD]; diameter range = 8–29 mm), which were detected by chest radiograph or CT performed on patients with suspicious of malignancy at nearby hospitals, prospectively underwent dynamic CT, dynamic MRI, FDG-PET, transbronchial or percutaneous biopsies, bronchoalveolar lavage, microbiological examinations, resection by thoracotomy, and video-assisted thoracic surgery (VATS) or follow-up MDCT examinations.

Patients were selected for this study according to the following criteria: 1) presence of pulmonary nodules <30 mm in diameter and without calcification; 2) no contraindications for the administration of gadolinium chelate and iodinated contrast media; and 3) ability to participate cooperatively in the procedures. Diameter was defined as the greatest diameter observed on conventional thin-section MDCT scans, which were obtained with a lung window setting. No calcification in pulmonary nodules meant absence of visible calcification on conventional thin-section MDCT scans (i.e., 1-mm section thickness) obtained with a mediastinal window setting. Each patient underwent dynamic MR, dynamic CT, and FDG-PET examinations within a three-week period (mean = 7.3 days; range = 4–18 days). Final diagnoses in all patients were confirmed by microbiological examination (N = 202), cytological or histological examinations of specimens obtained by CT-guided transthoracic needle biopsy (N = 9), transbronchial lung biopsy (N = 30), VATS (N = 28), or surgical resection (N = 135) and follow-up MDCT examinations (N = 39).

All nodules were classified into three groups based on the final diagnosis. The first group comprised malignant nodules (N = 152), which were subdivided into 146 primary peripheral lung cancers (77 adenocarcinomas with mixed bronchioloalveolar carcinoma [BAC] and other subtypes including acinar, papillary, or solid adenocarcinomas, 34 localized BACs, 22 adenocarcinomas without mixed subtypes, eight squamous cell carcinomas, and five large cell carcinomas) and six metastatic lung tumors consisting of three colon cancers, two renal cell carcinomas, and one thyroid cancer. The second group consisted of benign nodules (N = 39; 21 organizing pneumonias, 15 tuberculomas, and three hamartomas) and the third of active infectious nodules (N = 11; six atypical mycobacterium infections, two active tuberculoses, two aspergiloses, and one cryptococcosis). Tuberculomas were distinguished from active tuberculosis according to the following criteria: 1) no evidence of change in size at follow-up MDCT examinations every six months for more than two years; and 2) no evidence of the presence of microbacterium tuberculosis during microbacterial examination.

Dynamic MDCT Examinations

All dynamic MDCT studies were performed on a 16-detector CT scanner (Aquilion 16; Toshiba Medical Systems, Tokyo, Japan) as described elsewhere (8,9). For the routine chest CT of the entire lung, scans were obtained from the lung apex to the diaphragm during suspended respiration. Before the intravenous administration of contrast media for dynamic MDCT, a series

of 15 images was obtained through the nodule over a distance of 30 mm along the z-axis with the following parameters: collimation = 16 × 2 mm, 120 kV, 60 mA, gantry rotation time = 0.5 seconds, beam pitch = 1.44, and slice thickness reconstruction = 2 mm. This was followed by an additional five series of images obtained at 30, 60, 90, and 120 seconds and five minutes after intravenous injection of the contrast media (4 mL/seconds, total of 100 mL of Iopamiron 300, Iopamidol; Bayer Health Care, Osaka, Japan) with a power injector (Auto Enhance-60; Nemoto, Tokyo, Japan) and using the same parameters as those for the initial preenhancement series (total six series of images at t = 0 seconds, t = 30 seconds, t = 60 seconds, t = 90 seconds, t = 120 seconds, and t = 5 minutes). Image data were reconstructed with a thickness of 2.0 mm and a standard algorithm. The theory and basics of dynamic CT protocol were according to the previous literatures (8,9). Of the 175 patients, 13 had two pulmonary nodules and seven had three pulmonary nodules. Therefore, 20 patients underwent one or two additional dynamic MDCT examinations within two weeks (mean = 5.6 days, range = 3–10 days) after the initial dynamic MDCT examinations. All dynamic MDCT examinations were completed successfully without any adverse effects.

Dynamic MR Examinations

All MR studies were performed with a 1.5T superconducting magnet (Gyroscan Intera T-15; Philips Medical Systems, Best, The Netherlands) using a body-array coil. Dynamic MR images (TR = 2.7 msec/TE = 0.6 msec/flip angle = 40°, matrix size = 128 × 96, reconstructed matrix size = 256 × 192, rectangular field of view [FOV] = 350–400 × 245–280 mm) were acquired with a three-dimensional (3D) radio frequency spoiled gradient echo sequence without fat suppression pulse. All dynamic MR studies were performed with patients' arms placed above the head for reduction of partial phase FOV. A 3D-slab with a thickness of 110 mm included nodules detected on T2-weighted turbo spin-echo images of the entire lung, and was used with 11 partitions and using an overcontiguous slice in the coronal plane in a left-to-right phase-encoded direction, resulting in an effective partition thickness of 10 mm and real-phase encoding in the slice direction of six steps. Therefore, the spatial resolution of dynamic MRI was 1.4–1.6 mm × 1.3–1.5 mm × 10 mm, and the temporal resolution was 1.1 second for each 3D data set. The standard dose (0.1 mmol/kg body weight) of gadopentetate dimeglumine (Gd-DTPA, Magnevist; Bayer) was bolus administered to all patients via a cubital vein with an automatic infusion system (Sonic Shot, Nemoto) at a rate of 5 mL/second, followed by 20 mL of saline solution at the same rate. Dynamic MR sequence in each patient was initiated at the time of contrast media injection. The basic theory and application of contrast-enhanced dynamic MRI has been documented in previous publications (19,22).

Before the MR studies, patients were carefully instructed in the breathholding technique and practiced it to reproduce exactly the same degree of inspiration for each scan series. With each scan, 25 images were obtained during 28 seconds of breathholding at end-inspiration. All 175 dynamic MR examinations were completed successfully without any adverse effects.

FDG-PET Examinations

All FDG-PET examinations were performed with a commercially available PET scanner (Allegro; Philips). Patients fasted for at least six hours before the intravenous administration of FDG at a rate of 4.44 MBq/kg body weight, and imaging was performed from the skull through the midthigh 60 minutes after the injection. The 3D transmission scan was performed at a 23 seconds/bed position with Cesium-137 (^{137}Cs) point sources prior to FDG administration. Total duration of the ^{137}Cs transmission scan is about for minutes (100-cm scan length). The PET emission scan is automatically started at the end point of the transmission. The 3D emission scan consisted of eight to 11 bed positions of three minutes each (150 seconds/bed position), which made it possible to cover 770–1020 mm. Total acquisition time per patient varied from 30 to 40 minutes. The patients were given no specific breathing instructions, and scans were performed during quiet tidal breathing. PET images were reconstructed with the 3D Row Action Maximum Likelihood Algorithm (RAMLA) reconstruction algorithm (23) and displayed in a 144 × 144 matrix that contained 4.0 × 4.0 × 4.0 mm^3 voxels. After correction for radioactive decay, the SUV was calculated by dividing the administered FDG dose per kg of body weight for each voxel and displayed as the SUV image.

Image Analysis of Dynamic MDCT

All dynamic MDCT data were transferred to a personal computer (FMV-700), and regions of interest (ROIs) (diameter range = 8–29 mm) were placed over the pulmonary nodule by a chest radiologists with 13 years' experience (Y.O.) using the ImageJ Program 1.33u (Wayne Rasband, NIH, Bethesda, MD, USA). An ROI was placed over the tumor encompassing the entire cross-sectional area of the nodule, making it as large as possible to minimize the effects of tumoral hemodynamic inhomogeneities. All density-time curves of the tumor were generated on a mediastinal window setting to ensure that partial-volume averaging was minimized.

As described elsewhere (8,9), three wash-in parameters, namely, maximum enhancement, slope of enhancement, and net enhancement, and one wash-out parameter, absolute loss of contrast media, were calculated to characterize the pulmonary nodules. On all pulmonary nodules, each dynamic MDCT index was measured twice and averaged for the final value.

Maximum enhancement was defined as the maximum attenuation value of a nodule over the entire time-course of the dynamic study (8,9).

The net enhancement was calculated by using the following formula (8,9):

$$\text{Net enhancement} = \text{Maximum enhancement} - \text{Pre-enhancement attenuation value.} \quad [1]$$

The slope of enhancement was determined with the following equation (8,9):

$$\text{Slope of enhancement} = \text{Net enhancement} \div \text{Peak time (t)}, \quad [2]$$

where peak time (t) is the time at the maximum enhancement after bolus injection of the contrast agent. Maximum enhancement and peak time in each nodule were determined by visual inspection of the curve. The unit of measurement is expressed as Hansfield units (HU)/second. The slope of tumor enhancement also represents the first transit of the bolus contrast material (8,9,19,22).

Absolute loss of enhancement was calculated from the following equation (8,9):

$$\text{Absolute loss of enhancement} = \text{Maximum enhancement} - \text{Attenuation value at 5 min.} \quad [3]$$

Image Analysis of Dynamic MRI

All dynamic MR data were transferred to a same personal computer, and ROIs were placed over the normal lung parenchyma and pulmonary nodule by the same chest radiologist using the same image analysis software. An ROI was placed over the tumor encompassing the entire cross-sectional area of the nodule, making it as large as possible to minimize the effects of tumoral hemodynamic inhomogeneities. Signal intensity–time curves of nodule and normal lung parenchyma were generated. In each patient, ROI for measurement of signal intensity of normal lung parenchyma was placed at same lung field within contralateral lung on same coronal plane.

For our study and as previously described (19,22), two wash-in parameters such as maximum relative enhancement ratio and slope of enhancement ratio were calculated to characterize the pulmonary nodules. On each pulmonary nodule, both indices were measured twice and averaged to obtain the final ratios.

Maximum enhancement ratio was determined with the following formula:

$$\text{Maximum enhancement ratio} = (SI_{max} - SI_0) \div SI_0, \quad [4]$$

where SI_{max} is the maximum signal intensity after bolus injection of the contrast agent, and SI_0 is the signal intensity at baseline. The maximum enhancement ratio of the tumor can be normalized by that of the reference tissue (normal lung parenchyma) to generate the maximum relative enhancement.

The slope of the enhancement ratio was determined with the following equation:

$$\text{Maximum relative enhancement ratio} \div (\text{peak time [t]} - \text{start time [t]}), \quad [5]$$

where peak time [t] is the time at the maximum signal intensity after bolus injection of the contrast agent, and start time [t] indicates the beginning of the continuous contrast enhancement effect of pulmonary nodule. Peak and start times in each nodule were determined by visual inspection of the curve. The value is expressed in seconds^{-1} (per second). The slope of the enhancement ratio of the tumor represents the first transit of the bolus contrast material (19,22).

Automated Coregistration of FDG-PET and CT Images and Image Analysis of Coregistered PET/CT

All pre-contrast-enhanced CT data, reformatted to a 256 × 256 matrix, were transferred to a personal computer (FMV-900; Fujitsu) and coregistered with SUV image data from FDG-PET by using a commercially available software (NEUROSTAT; Nihon Medi-Physics Co., Ltd., Nishinomiya, Japan). This software is fully-automated 3D registration software using a rigid body transformation technique, and has been described previously (24,25). For FDG-PET/CT images, SUV data were overlaid on conventional plain MDCT with the lung window set for a FDG-PET/CT section thickness of 5 mm. ROIs (diameter range = 8–29 mm) were then placed over the pulmonary nodule for determination of maximum value of SUV (SUV_{max}) by the same chest radiologist using the same software. An ROI was placed over the tumor encompassing the entire cross-sectional area of the nodule, making it as large as possible. On each pulmonary nodule, SUV_{max} was measured twice and averaged to obtain the final value.

Statistical Analysis

Intraobserver Variabilities of Dynamic MDCT Indices, Dynamic MR Indices, and SUV_{max}

To compare intraobserver variability among dynamic MDCT and MR indices and SUV_{max}, correlation between first and second measurements and reproducibility coefficient of each index were analyzed by Bland-Altman analysis (26).

Difference Among Malignant, Benign, and Active Infectious Nodules

To identify the differences among malignant, benign, and active infectious nodules, the largest diameter, dynamic MDCT indices, dynamic MR indices, and SUV_{max} were compared among the three types of nodules by using Tukey's honestly significant difference (HSD) test.

Capability of Three Modalities for Differentiation of Malignant From Benign Nodules

To compare capability for distinguishing malignant (malignant nodules) from benign pulmonary nodule (benign and active infectious nodules) groups among wash-in parameters from dynamic MDCT and MR indices and SUV_{max} from PET/CT, receiver operating characteristics (ROC) curve analyses were performed, and the feasible threshold values as markers for the malig-

nant nodule group were also determined. In true- and false-positive nodules assessed by using each of the wash-in indices of the dynamic MDCT, the feasible threshold value of the wash-out parameter for a decreasing false-positive rate could be determined without a significant reduction in true-positive cases as compared with results obtained with dynamic MR indices and SUV_{max} from scattergrams. Final sensitivities, specificities, and accuracies for distinguishing malignant from benign pulmonary nodules of combined wash-in and wash-out parameters for dynamic MDCT, and of both wash-in parameters for dynamic MRI and SUV_{max} were compared by means of the McNemar's test.

Capabilities of Three Modalities for Distinguishing Pulmonary Nodules Requiring Further Intervention and Treatment From Pulmonary Nodules Requiring No Further Evaluation

To compare capability for distinguishing pulmonary nodules requiring further intervention and treatment (malignant and active infectious nodules) from pulmonary nodules requiring no further evaluation (benign nodules) groups among wash-in parameters from dynamic MDCT and MR indices and SUV_{max} from PET/CT, ROC analyses were performed, and the feasible threshold values as markers for the pulmonary nodule requiring further intervention and treatment group were also determined. When a wash-out parameter reduced the false-positive nodules of each of the wash-in indices of dynamic MDCT without significant reduction of true-positive cases as compared with results obtained with dynamic MR indices and SUV_{max} from scattergrams, the feasible threshold value of the wash-out parameter for each of the wash-in indices was also determined. Finally, these threshold values were then tested to determine the capability of each index for distinguishing pulmonary nodules requiring further intervention and treatment from those requiring no further evaluation by the McNemar's test.

P values <0.05 were considered as statistically significant for all statistical analyses.

RESULTS

One representative case each of the malignant nodule, benign nodule, and active infectious nodule groups is shown in Figs. 1, 2, and 3.

Intraobserver Variabilities of Dynamic MDCT Indices, Dynamic MR Indices, and SUV_{max}

Correlation between first and second measurements, mean difference between first and second measurements, and reproducibility coefficient of each index are shown in Table 1. There was significant and excellent correlation between first and second measurements of dynamic MDCT and MR indices and SUV_{max} ($0.96 \leq r \leq 0.98$, $P < 0.0001$). Mean difference of maximum enhancement, net enhancement, slope of enhancement, absolute loss of enhancement, maximum relative enhancement ratio, slope of enhancement ratio, and SUV_{max} between first and second measurements were almost 0 (maximum enhancement = 0.3 HU, net enhancement = 0.1 HU, slope of enhancement = −0.05 HU/second, absolute loss of enhancement = −0.5 HU, maximum relative enhancement ratio = 0.00, slope of enhancement ratio = −0.03/second, and SUV_{max} = 0.01), and small enough for clinical purposes. Reproducibility coefficients of maximum enhancement (7.6 HU), net enhancement (3.0 HU), slope of enhancement (0.10 HU/second), absolute loss of enhancement (4.6 HU), maximum relative enhancement ratio (0.06), slope of enhancement ratio (0.008/second), and SUV_{max} (0.12) between first and second measurements were also small enough for clinical purposes.

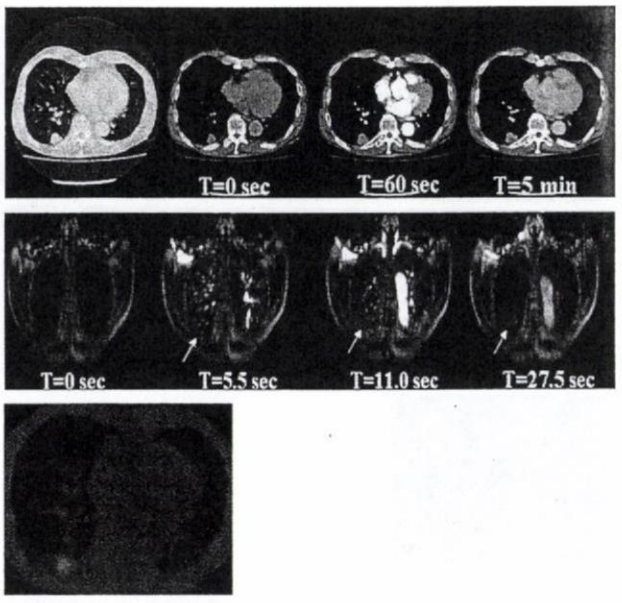

Figure 1. A 79-year-old male with primary lung cancer (adenocarcinoma) in the right lower lobe. **a:** Routine CT shows a nodule with a diameter of 25 mm in the right lower lobe. T indicates the time after bolus injection of contrast media. On dynamic CT, maximum enhancement, net enhancement, slope of enhancement, and absolute loss of enhancement are 73.2 HU, 32.4 HU, 0.54 HU/second, and 10.7 HU, respectively. This case is true-positive on dynamic CT indices. **b:** Dynamic MR images demonstrate enhancement of the nodule (arrow). T indicates the time after bolus injection of contrast media. Maximum relative enhancement ratio is 0.36 and slope of enhancement ratio is 0.065/second. This case is true-positive on both dynamic MR indices. **c:** Coregistered PET/CT demonstrates high uptake of FDG, and SUV_{max} of the lesion is 3.8. This case is true-positive on coregistered PET/CT.

Difference Among Malignant, Benign, and Active Infectious Nodules

Long-axis diameter, dynamic CT indices, dynamic MR indices, and SUV_{max} for the three groups are shown in Table 2. Means of maximum enhancement, net enhancement, slope of enhancement, absolute loss of enhancement, maximum relative enhancement ratio, slope of enhancement ratio, and SUV_{max} of malignant nodules were significantly different from those of benign nodules ($P < 0.05$). Means of maximum enhancement, net enhancement, absolute loss of enhancement,

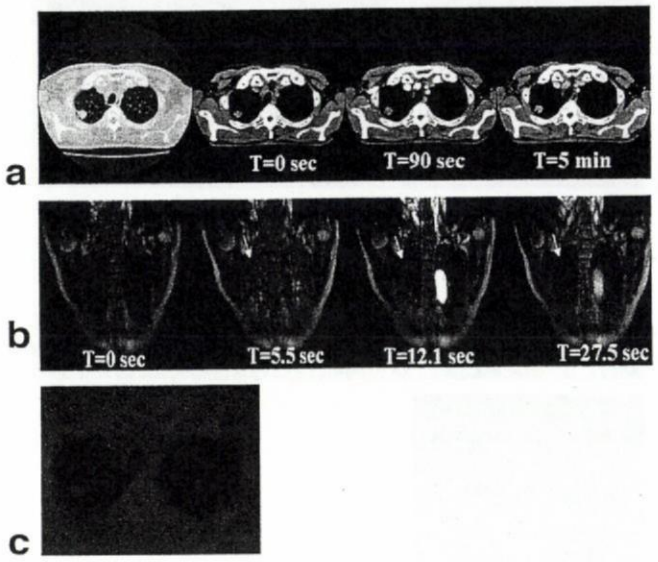

Figure 2. A 70-year-old male with organizing pneumonia in the right upper lobe. **a:** Routine CT shows a nodule with diameter of 22 mm in the right upper lobe. T indicates the time after bolus injection of contrast media. On dynamic CT, maximum enhancement, net enhancement, slope of enhancement, and absolute loss of enhancement are 66.4 HU, 25.4 HU, 0.28 HU/second, and 8 HU, respectively. This case is false-positive on maximum enhancement or net enhancement combined with absolute loss of enhancement. **b:** Dynamic MR images demonstrate enhancement of the nodule (arrow). T indicates the time after bolus injection of contrast media. Maximum relative enhancement ratio is 0.17 and slope of enhancement ratio is 0.011/second. This case is true-negative on both dynamic MR indices. **c:** Coregistered PET/CT demonstrates high uptake of FDG, and SUV_{max} of the lesion is 1.5. This case is true-negative on coregistered PET/CT.

maximum relative enhancement ratio, slope of enhancement ratio, and SUV_{max} of active infectious nodules were also significantly different from those of benign nodules ($P < 0.05$). Moreover, absolute loss of enhancement and slope of enhancement ratio of the malignant nodule group were significantly different from those of the active infection groups ($P < 0.05$).

Capability of Three Modalities for Differentiation of Malignant From Benign Nodules

The results of ROC analyses of wash-in parameters for dynamic CT, both dynamic MR indices and SUV_{max} on PET/CT for distinguishing malignant nodule from benign nodules are shown in Fig. 4. Area under the curve (Az) of slope of enhancement (Az = 0.75, $P < 0.05$) had significant difference with maximum relative enhancement ratio (Az = 0.87), slope of enhancement ratio (Az = 0.85), and SUV_{max} (Az = 0.87).

Feasible threshold values of maximum enhancement, net enhancement, slope of enhancement, maximum relative enhancement ratio, slope of enhancement ratio, and SUV_{max} were determined as follows: 60 HU, 20 HU, 0.4 HU/second, 0.2, 0.04/second, and 1.8.

2D scattergrams for each of the wash-in parameters of dynamic CT and absolute loss of enhancement of all cases are shown in Fig. 5. To improve the diagnostic capability of each wash-in parameter on dynamic CT, the feasible threshold value for absolute loss of enhancement was determined as equal to or less than 30 HU. When this threshold value was adopted, active infectious nodules were not included in the false-positive nodules.

The feasible threshold values, final sensitivities, specificities, positive predictive values, negative predictive values, and accuracies of dynamic MDCT, dynamic MRI, and PET/CT are shown in Table 3. When the feasible threshold value for each of the indices was adapted, accuracy of the maximum relative enhancement ratio was significantly higher than that of maximum enhancement and absolute loss of enhancement combined or of the slope of enhancement and absolute loss of enhancement combined ($P < 0.05$). Specificity of the maximum relative enhancement ratio was also significantly higher than that of maximum enhancement and absolute loss of enhancement combined ($P < 0.05$). Accuracy of the slope of enhancement ratio was significantly higher than that of all dynamic CT indices combined with absolute loss of enhancement and SUV_{max} ($P < 0.05$). Specificity of the slope of enhancement ratio was also significantly higher than that of all dynamic CT indices and absolute loss of enhancement combined ($P < 0.05$).

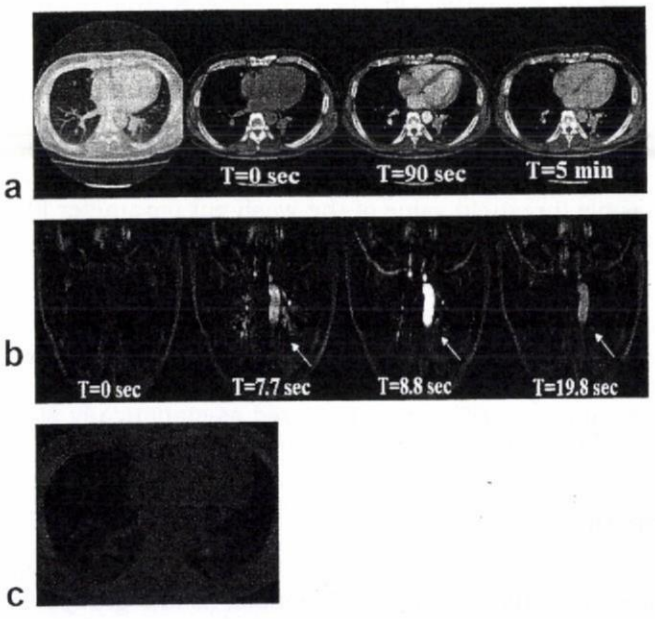

Figure 3. A 61-year-old male with aspergilloma in the left lower lobe. **a:** Routine CT shows a nodule with a diameter of 27 mm in the left lower lobe. T indicates the time after bolus injection of contrast media. On dynamic CT, maximum enhancement, net enhancement, slope of enhancement, and absolute loss of enhancement are 79.9 HU, 36.8 HU, 0.41 HU/second, and 9 HU, respectively. This case is false-positive on dynamic CT indices. **b:** Dynamic MR images demonstrate enhancement of the nodule (arrow). T indicates the time after bolus injection of contrast media. Maximum relative enhancement ratio is 0.42 and slope of enhancement ratio is 0.038/second. This case is false-positive according to maximum relative enhancement ratio and true-negative according to slope of enhancement ratio. **c:** Coregistered PET/CT demonstrates high uptake of FDG, and SUV_{max} of the lesion is 4.5. This case is false-positive on coregistered PET/CT.

Table 1
Correlation, Mean Difference, and Reproducibility Coefficient of Each Index Between First and Second Measurements

	Correlation between first and second measurement		Mean difference between first and second measurements	Reproducibility coefficient
	r	*P* value		
Maximum enhancement	0.98	<0.0001	0.3 HU	7.6 HU
Net enhancement	0.98	<0.0001	0.1 HU	3.0 HU
Slope of enhancement	0.97	<0.0001	−0.05 HU/second	0.10 HU/second
Absolute loss of enhancement	0.96	<0.0001	−0.5 HU	4.6 HU
Maximum relative enhancement ratio	0.98	<0.0001	0.00	0.06
Slope of enhancement ratio	0.98	<0.0001	−0.03/second	0.008/second
SUV_{max}	0.98	<0.0001	0.01	0.12

Finally, specificity and accuracy of SUV_{max} were significantly higher than those of maximum enhancement and absolute loss of enhancement combined ($P < 0.05$).

Capabilities of Three Modalities for Distinguishing Pulmonary Nodules Requiring Further Intervention and Treatment From Pulmonary Nodules Requiring No Further Evaluation

The results of results of ROC analyses of wash-in parameters for dynamic CT, both dynamic MR indices, and SUV_{max} on PET/CT as markers for distinguishing pulmonary nodules requiring further intervention and treatment from those requiring no further evaluation are shown in Fig. 6. Az's of maximum relative enhancement ratio (Az = 0.96), slope of enhancement ratio (Az = 0.97), and SUV_{max} (Az = 0.96) were significantly different from that of slope of enhancement (Az = 0.87, $P < 0.05$).

The feasible threshold values of maximum enhancement (60 HU), net enhancement (20 HU), slope of enhancement (0.4 HU/second), maximum relative enhancement ratio (0.2), slope of enhancement ratio (0.04/second), and SUV_{max} (1.8) were the same those for distinguishing malignant pulmonary nodules from others. As demonstrated by the scattergram in Fig. 5, the feasible threshold value of the wash-out parameter of dynamic MDCT could not be determined without a significant reduction in sensitivity, specificity, and/or accuracy for distinguishing pulmonary nodules requiring further intervention and treatment from those requiring no further evaluation.

The feasible threshold values, sensitivity, specificity, positive predictive value, negative predictive value, and accuracy for distinguishing the two groups of pulmonary nodules by dynamic MDCT, dynamic MRI, and PET/CT are shown in Table 4. The respective specificities and accuracies of maximum enhancement ratio, slope of enhancement ratio, and SUV_{max} were significantly higher than those of all dynamic CT indices ($P < 0.05$). Specificity and accuracy of the slope of enhancement ratio were significantly higher than those of the maximum enhancement ratio and SUV_{max} ($P < 0.05$).

DISCUSSION

Our results show significant and reproducible differences in the dynamic CT and MR indices and SUV_{max} among the malignant, benign, and active infectious nodule groups. They also indicate that dynamic MRI and coregistered PET/CT can differentiate more specifically and accurately than dynamic MDCT between the malignant pulmonary nodule group (malignant nodule) and the benign pulmonary nodule group (benign and active infectious nodules), and distinguish more specifically and accurately pulmonary nodules requiring further intervention and treatment (malignant and active infectious nodules) from those requiring no further

Table 2
Parameters of Malignant, Benign, and Active Infectious Nodules

Parameters	Malignant nodules ($N = 152$) mean ± SD (range)	Benign nodules ($N = 39$) mean ± SD (range)	Active infectious nodules ($N = 11$) mean ± SD (range)
Long-axis diameter (mm)	16.1 ± 6.3 (8–29)	14.4 ± 4.6 (6–29)	15.3 ± 5.6 (8–28)
Maximum enhancement (HU)	106.7 ± 29.5 (40–164.7)	63.7 ± 20.5[a,b] (35–117)	102.0 ± 24.9 (60.3–135.9)
Net enhancement (HU)	64.5 ± 27.9 (8.6–117.8)	24.0 ± 15.5[a,b] (6.5–57.4)	56.1 ± 23.8 (15.2–89.6)
Slope of enhancement (HU/second)	1.08 ± 0.46 (0.13–1.98)	0.54 ± 0.46[a] (0.02–1.67)	0.91 ± 0.63 (0.19–1.95)
Absolute loss of enhancement (HU)	14.7 ± 7.0 (2.8–35.7)	8.1 ± 4.0[a,b] (1.9–18.5)	28.5 ± 8.6[a] (5.0–37.8)
Maximum relative enhancement ratio	0.51 ± 0.17 (0.04–0.85)	0.17 ± 0.09[a,b] (0.04–0.37)	0.45 ± 0.13 (0.24–0.67)
Slope of enhancement ratio (per second)	0.11 ± 0.04 (0.01–0.25)	0.02 ± 0.03[a,b] (0.01–0.10)	0.14 ± 0.04[a] (0.11–0.22)
SUV_{max}	4.4 ± 1.8 (0.8–7.8)	1.4 ± 1.1[a,b] (0.2–5.3)	3.5 ± 1.2 (1.1–5.6)

[a]Significant difference from malignant nodules ($P < 0.05$).
[b]Significant difference from active infectious nodules ($P < 0.05$).
SD, standard deviation.